Structural and photosynthetic dynamics mediate the response of SIF to water stress in a potato crop

Xu, Shan

2021-09-15

Xu , S , Atherton , J , Riikonen , A , Zhang , C , Oivukkamaki , J , MacArthur , A , Honkavaara , E , Hakala , T , Koivumaki , N , Liu , Z & Porcar-Castell , A 2021 , ' Structural and photosynthetic dynamics mediate the response of SIF to water stress in a potato crop ' , Remote Sensing of Environment , vol. 263 , 112555 . https://doi.org/10.1016/j.rse.2021.112555

http://hdl.handle.net/10138/339544
https://doi.org/10.1016/j.rse.2021.112555

Remote Sensing of Environment 263 (2021) 112555

Contents lists available at ScienceDirect

Remote Sensing of Environment

journal homepage: www.elsevier.com/locate/rse

Structural and photosynthetic dynamics mediate the response of SIF to water stress in a potato crop

Shan Xu [a,b,c,*], Jon Atherton [a], Anu Riikonen [a], Chao Zhang [a], Jaakko Oivukkamäki [a], Alasdair MacArthur [d], Eija Honkavaara [e], Teemu Hakala [e], Niko Koivumäki [e], Zhigang Liu [b,c], Albert Porcar-Castell [a,**]

[a] Optics of Photosynthesis Laboratory, Institute for Atmospheric and Earth System Research/Forest Sciences, Viikki Plant Science Center, University of Helsinki, 00014 Helsinki, Finland
[b] State Key Laboratory of Remote Sensing Science, Jointly Sponsored by Beijing Normal University, Institute of Remote Sensing and Digital Earth of Chinese Academy of Sciences, 100875 Beijing, China
[c] Beijing Engineering Research Center for Global Land Remote Sensing Products, Institute of Remote Sensing Science and Engineering, Faculty of Geographical Science, Beijing Normal University, 100875 Beijing, China
[d] NERC Field Spectroscopy Facility, School of Geosciences, University of Edinburgh, EH8 9AB Edinburgh, UK
[e] Department of Remote Sensing and Photogrammetry, Finnish Geospatial Research Institute, National Land Survey of Finland, Geodeetinrinne 2, 02431 Masala, Finland

ARTICLE INFO

Editor name: Jing M. Chen

Keywords:
Solar-induced chlorophyll fluorescence
Gross primary production
Leaf angle distribution
Water stress

ABSTRACT

Solar-induced Fluorescence (SIF) has an advantage over greenness-based Vegetation Indices in detecting drought. This advantage is the mechanistic coupling between SIF and Gross Primary Productivity (GPP). Under water stress, SIF tends to decrease with photosynthesis, due to an increase in non-photochemical quenching (NPQ), resulting in rapid and/or sustained reductions in the fluorescence quantum efficiency (Φ_F). Water stress also affects vegetation structure via highly dynamic changes in leaf angular distributions (LAD) or slower changes in leaf area index (LAI). Critically, these responses are entangled in space and time and their relative contribution to SIF, or to the coupling between SIF and GPP, is unclear. In this study, we quantify the relative effect of structural and photosynthetic dynamics on the diurnal and spatial variation of canopy SIF in a potato crop in response to a replicated paired-plot water stress experiment. We measured SIF using two platforms: a hydraulic lift and an Unmanned Aerial Vehicle (UAV) to capture temporal and spatial variation, respectively. LAD parameters were estimated from point clouds and photographic data and used to assess structural dynamics. Leaf Φ_F estimated from PAM fluorescence measurements were used to represent variations in photosynthetic regulation. We also measured foliar pigments, operating quantum yield of photosystem II (PSII), photosynthetic gas exchange, stomatal conductance and LAI. We used a radiative transfer model (SCOPE) to provide a means of decoupling structural and photosynthetic factors across the diurnal and spatial domains. The results demonstrate that diurnal variation in SIF is driven by photosynthetic and structural dynamics. The influence of Φ_F was prominent in the diurnal SIF response to water stress, with reduced fluorescence efficiencies in stressed plants. Structural factors dominated the spatial response of SIF to water stress over and above Φ_F. The results showed that the relationship between SIF and GPP is maintained in response to water stress where adjustments in NPQ and leaf angle co-operate to enhance the correlation between SIF and GPP. This study points to the complexity of interpreting and modelling the spatiotemporal connection between SIF and GPP which requires simultaneous knowledge of vegetation structural and photosynthetic dynamics.

* Corresponding author at: No.19, Xinjiekouwai St, Haidian District, Beijing 100875, PR China.
** Corresponding author at: Optics of Photosynthesis Laboratory, Institute for Atmospheric and Earth System Research/Forest Sciences, University of Helsinki, PO Box 27, 00014, Finland.
E-mail addresses: bnuxushan@gmail.com (S. Xu), joan.porcar@helsinki.fi (A. Porcar-Castell).

https://doi.org/10.1016/j.rse.2021.112555
Received 25 November 2020; Received in revised form 6 April 2021; Accepted 3 June 2021
Available online 23 June 2021

1. Introduction

Climate change poses several risks to agriculture, with drought identified as the single most important factor potentially limiting crop production in Europe (Olesen et al., 2011). Consequently, there is an urgent need for remote sensing products that quantify the impact of drought on productivity. Present insight into drought effects on productivity has been gained by fusing vegetation indices (VIs), representing so called canopy greenness, with climatological dryness indicators such as the Palmer drought severity index (Alley, 1984). This combined approach has been used to estimate drought severity across space (Wardlow et al., 2012) and to quantify historical decreases in productivity on decadal time scales (Zhang et al., 2016). The main limitation of this approach is that greenness-based VIs do not capture shorter timescale changes in productivity that occur during a drought episode, as greenness potentially decouples from productivity at these scales.

Unlike greenness-based VIs, solar-induced fluorescence (SIF) does respond near-instantaneously to rapid adjustments in the photosynthetic machinery (Porcar-Castell et al., 2014). Therefore researchers have begun to investigate the use of remote sensing retrievals of SIF for the detection of drought and water stress in crops. Zarco-Tejada et al. (2009) flew an Unmanned Aerial Vehicle (UAV) imaging spectroscopy platform to demonstrate a photosynthesis related SIF response to water stress in fruit trees. Using satellite data, Sun et al. (2015) found strong negative anomalies in SIF that captured large scale drought development across the USA. Sun et al. (2015) suggested that the response of SIF to extreme drought may be due to rapid photosynthetic related reductions in SIF, but also to canopy structure factors such as leaf wilting. Following from this, Zhang et al. (2019) found increased sensitivity of satellite SIF to drought in crops in Australia, relative to broadband VIs, suggesting that SIF could potentially be used as an improvement on the present drought detection approach.

In contrast to the larger scale, where SIF is emerging as a reliable indicator of drought, evidence of leaf and canopy scale mechanisms to support this use is weaker. Although early work did show changes in steady state chlorophyll fluorescence (ChlF) in response to water stress, ChlF was measured with active fluorometers (Flexas et al., 2002), and nonlinear and species dependencies were noted between ChlF and stomatal conductance. Helm et al. (2020) followed up on the earlier work with leaf level SIF instrumentation, and found that large drought-related reductions in net photosynthesis were followed by relatively smaller reductions in SIF. Also recently, Marrs et al. (2020) did not find consistent decreases in SIF following stomatal closure and related photosynthetic reductions in experimentally manipulated deciduous trees over a single day. These experimental results suggest that although SIF does respond to drought, the response may be weak. Hence there is an inconsistency between the satellite SIF evidence, which clearly captures drought over and above the VIs, and leaf scale studies which suggest a muted response.

ChlF is an emission of electromagnetic radiation in the red and far-red region of the spectrum by photosynthetic chlorophyll-containing predominantly leaf tissues exposed to visible light (Baker, 2008; Porcar-Castell et al., 2014). However, as satellite SIF retrievals of ChlF do not resolve individual leaves, the impact of canopy structure must be taken into account in addition to photosynthetic factors (Guanter et al., 2014). At the canopy scale, the biophysical processes of SIF can be represented using a simple equation:

$$SIF = APAR \times \Phi_F \times f_{esc} \quad (1)$$

where APAR is absorbed photosynthetically active radiation (PAR) by green leaves which is decomposed into the product of the fraction of absorbed incident radiation (fPAR) and incident PAR (APAR = fPAR × PAR). Φ_F is the fluorescence efficiency at the canopy level, and f_{esc} is the probability that an emitted photon will escape the canopy in the direction of the sensor, i.e. the escape probability (Guanter et al., 2014; Huang et al., 2007; Zeng et al., 2019). Eq. (1) can be used to recast Monteith's (1972) light use efficiency model in terms of SIF, as:

$$GPP = APAR \times LUE \quad (2)$$

where LUE is light use efficiency and defined as the ratio of Gross Primary Productivity (GPP) to APAR, then from simple algebra we can combine Eq. (1) and Eq. (2) to arrive at the following expression:

$$GPP = \frac{LUE}{\Phi_F} \times \frac{1}{f_{esc}} \times SIF \quad (3)$$

Eq. (3) demonstrates that the relationship between GPP and SIF depends on both structural factors (f_{esc}) and photosynthetic factors (Φ_F, LUE) (Dechant et al., 2020; Martini et al., 2019; Zhang et al., 2020).

Whereas LUE integrates the effect of dynamic responses across the whole photosynthetic process, Φ_F responds to changes in light energy partitioning at the level of the light reactions of photosynthesis. Light energy absorbed by photosynthetic pigments has three main dissipating pathways: photosynthesis (or photochemical quenching, PQ), non-radiatively as heat (or non-photochemical quenching, NPQ) and fluorescence. Under limiting light conditions and in the absence of sustained stress, Φ_F is mostly controlled by PQ. Then Φ_F and the operating quantum yield of photochemistry in PSII (Φ_P) are inversely related (Alonso et al., 2017; Porcar-Castell et al., 2014; Van der Tol et al., 2014). As radiation increases, or under stress conditions, the carbon reactions of photosynthesis gradually become light saturated and NPQ mechanisms are activated. Under these conditions, both Φ_P and Φ_F decrease proportionally under the action of NPQ (Frankenberg and Berry, 2018; Porcar-Castell et al., 2014; Van der Tol et al., 2014).

The regulatory action of NPQ is the mechanistic connection between Φ_F and LUE, that remote sensing of photosynthesis using SIF is precipitated on. Critically, in addition to the interfering effect of PQ dynamics described above, the relationship between Φ_F and LUE is further complicated by the dynamics of alternative energy sinks which compete for photosynthetic electron transport with GPP, reducing LUE, but which do not necessarily affect Φ_F (Maxwell and Johnson, 2000; Porcar-Castell et al., 2014). Such interferences are expected in response to water stress, where stomatal closure results in an increase in the internal concentration of O_2 relative to that of CO_2, promoting the oxygenation of RuBisCO (Ribulose-1,5-bisphosphate carboxylase/oxygenase) at the expense of carboxylation in a process described as photorespiration (Flexas et al., 2000), which results in decreased LUE. Accordingly, and although Φ_F has been repeatedly shown to decrease in response to water stress due to increasing levels of NPQ (Cendrero-Mateo et al., 2015; Flexas et al., 2002; Flexas et al., 2000; Magney et al., 2019b), factors such as photorespiration could dampen the relationship and explain the recent experimental results (Helm et al., 2020; Marrs et al., 2020).

To quantify the response of SIF to drought at scales larger than a leaf requires understanding of canopy structural parameters that encapsulate canopy radiative transfer processes and mechanisms. Multiple scattering and reabsorption of emitted SIF is parameterized using f_{esc}, which is related to structure, gap fraction, reabsorption, but also viewing and illumination geometry, and is dynamic across time and space. The near-infrared reflectance of vegetation (NIRv) and fluorescence correction vegetation index (FCVI) can be used to estimate f_{esc} from reflectance measurements (Yang et al., 2020; Zeng et al., 2019). Once estimated, f_{esc} can be used to correct observed SIF to total emitted SIF, which when combined with knowledge of APAR provides a method to retrieve Φ_F remotely via Eq. (1).

In addition to facilitating the remote retrieval of Φ_F, the structural parameters, APAR and f_{esc}, play a critical role in the relationship between GPP and SIF in crops (Miao et al., 2018; Yang et al., 2021). Dechant et al. (2020) conducted a re-analysis of crop datasets and found that variability in structural factors explained the relationship between SIF and GPP, over and above Φ_F, in rice, wheat and corn. Dechant et al.'s

(2020) study provides solid evidence for the marginal role of Φ_F driving the seasonality of SIF in crops growing under optimal conditions; however the role of Φ_F under plant stress, exemplified by drought, is uncertain. There is also the dichotomy between the satellite SIF evidence which demonstrates a strong drought response, and the contrasting results from the leaf level studies discussed earlier (Helm et al., 2020; Marrs et al., 2020). Resolving this scale dichotomy, especially for non-woody crops, requires concurrent observations of structural and photosynthetic dynamics under stress conditions, and a questioning of the assumptions on which our current understanding of the stress response of SIF rests. Such an effort may go some way to explaining differences in the linearity of SIF-GPP observed across studies which are rooted in the spatial and temporal context of the measurements (Magney et al., 2020).

The importance of leaf inclination angles in modulating the SIF signal is well known, yet little studied especially at shorter time-scales (Dechant et al., 2020; Pinto et al., 2017). Leaf and canopy movements in non-woody crops, such as potato, are wide-ranging and occur for many reasons including drought driven changes in turgor and circadian rhythms (Inoue et al., 2018; Treshow, 1970). Therefore, if we are to use SIF to follow the impacts of drought in crops, a simultaneous evaluation of the response of SIF to photosynthetic and structural factors is required, with both of these groupings considered dynamic in time and space. Only then can we reveal the mechanisms behind the drought response of SIF retrieved from space (Sun et al., 2015; Zhang et al., 2019).

We use a water stress experiment in a potato crop as a case study to quantify the relative effect of photosynthetic and structural factors on the spatiotemporal variation of top of canopy (TOC) SIF. Potato was used for two reasons, firstly potato is an economically important crop across Northern Europe (Walker et al., 1999), and secondly, the leaves of potatoes have the capacity for a relatively large degree of movement under the regulation of the circadian clock (Inoue et al., 2018; Yanovsky et al., 2000). Additionally, and as with most non-woody plants, leaf and shoot inclination angle are particularly sensitive to water potential due to changes in turgor (Treshow, 1970). Hence potato's potential for considerable diurnal shoot and leaf movements, observable through changes in leaf inclination angle, parameterized as the Leaf Angular Distribution (LAD) in the remote sensing literature, provided an ideal model species.

To decouple the effect of structure and photosynthetic factors on SIF we carried out a replicated paired sampling design water stress experiment on the potato crop. We used hydraulic lift and Unmanned Aerial Vehicle (UAV) measurement platforms to measure diurnal and spatial variation in SIF, as induced by the water stress treatment. We combined these observations with a comprehensive suite of field and proximal measurements including LAD and Φ_F and Soil-Canopy Observation Photosynthesis and Energy fluxes (SCOPE) (Van der Tol et al., 2009) model simulations to address the following three objectives: (i) to reveal the relative contribution of LAD and Φ_F on the daily pattern of variation in TOC SIF; (ii) to reveal the relative contribution of LAD and Φ_F on the spatial variation in TOC SIF; and (iii) to determine the impact of LAD and Φ_F dynamics on the relationship between GPP and TOC SIF during water stress.

2. Materials and methods

2.1. Experimental protocol and design

A water stress experiment was conducted at the Viikki campus (University of Helsinki) experimental field site, Finland (60.2269° N, 25.0186° E), in the summer of 2018 on potatoes (*Solanum tuberosum* L., variety 'Lady Felicia'). A 6 × 6 m split-plot design with five replicates was used, which resulted in a total of 10 plots which were labelled W1-W10 (Fig. 1). Potato (4000 kg/ha, rows 70 cm apart) was planted on 23 May and irrigated with 50 mm during the first two weeks using regular sprinklers. Potato shoots emerged on 11 June, and received an additional 50 mm over the three weeks through natural rainfall. Irrigation treatments were randomly imposed on 2 July with five irrigated (control, c) and five drought plots (treatment, t), where control plots were irrigated with 50 mm on the first week and 10 mm on the second week using furrow irrigation with a hose, whereas treatments were not irrigated for a period of two weeks. Rainfall during the drought experiment period was ca. 10 mm. July 2018 was unusually warm in Helsinki, with average temperature of 21.1 °C versus 30-year average of 17.8 °C (www.fmi.fi). Proximal sensing and field data collection were conducted on 17 and 18 July. To capture diurnal and spatial variation in TOC SIF, we used hydraulic lift and UAV platforms with the same optical instrument payload.

2.2. Proximal sensing spectroscopy and SIF retrieval

A dual field-of-view system composed of two spectrometers (Piccolo Doppio, PD) was used to measure canopy reflectance and SIF (Atherton et al., 2018; Porcar-Castell et al., 2015; MacArthur et al., 2014). A QE Pro spectrometer (Ocean Insight Inc., Dunedin, FL, USA) was used for

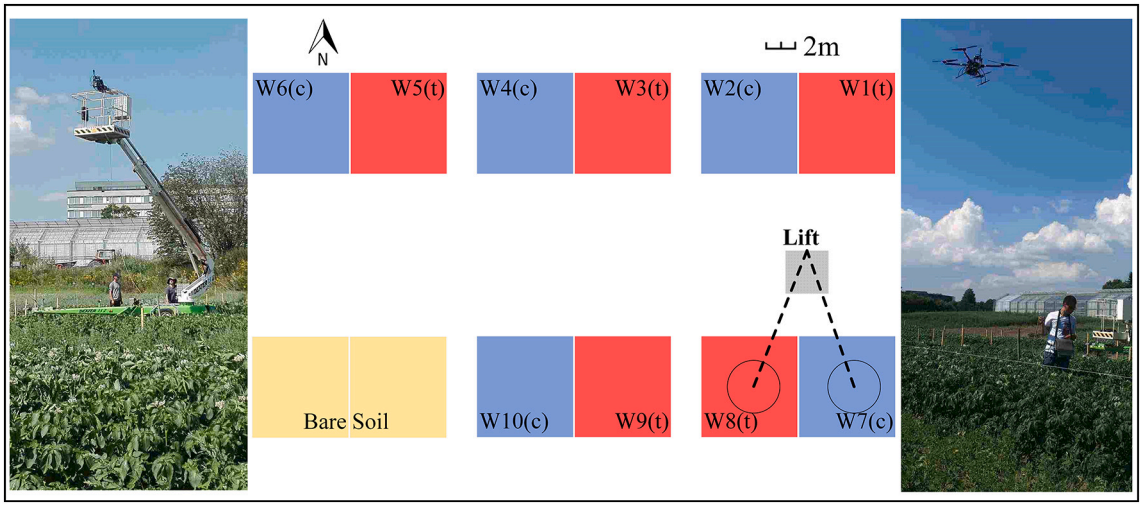

Fig. 1. Scheme of our water exclusion paired-plot experimental design (c, irrigated control; t, water stress treatment) with images of the lift and UAV platforms used for spectral measurements at approxomately 8 m height above the canopy. Diurnal measurement using lift platform was conducted in W7(c) and W8(t). The black circle illustrates the approximated footprint of the down-looking sensor. Spatial measurements with the UAV platform were conducted in all plots.

SIF retrieval, with FWHM of 0.31 nm, spectral sampling interval of 0.16 nm, and spectral range of 640–800 nm. A Flame spectrometer (Ocean Insight Inc., Dunedin, FL, USA) was used to estimate canopy reflectance in the visible to near-infrared range and derive vegetation indices, with FWHM of 1.3 nm, spectral sampling interval of 0.33 nm, and spectral range of 340–1000 nm. The PD system collects incident irradiance through a cosine corrected diffuser fore-optic attached to one fiber optic leg and upwelling radiance through a down-looking bare optic fiber with a field-of-view of 25°.

2.2.1. Measurements of diurnal and spatial SIF dynamics

The diurnal dynamics of SIF were measured on 18 July with the PD system attached to a rotatable hydraulic lift at a height approximately 8 m above canopy, which yielded a footprint radius approximately 1.77 m as viewed in the nadir direction. Measurements were switched between control and treatment plot by rotating the lift every 20 min. Data were collected in batches of 20 measurements which were bookended by dark current measurements collected with the integrated electronic shutter system of the PD and subsequently averaged. The integration times of spectrometers were automatically optimized based on brightness for upwelling and downwelling radiance. During diurnal measurements, the integration times of the QE pro spectrometer for the upwelling and downwelling radiation measurements were between 0.18 and 0.34 s, and 0.34–0.55 s, respectively. The PD system had a small tilt compared to nadir direction because of drift in the hydraulic system of the lift. The small tilt resulted in an irradiance error that depended on the horizontal location of the lift platform. We developed and applied a simple tilt correction method to compensate for this error using a nearby PAR sensor which is described in Appendix A. We assumed a negligible (pseudo-Lambertian) radiance (L) tilt effect.

The spatial dynamics of SIF were measured on the 17 July with the same PD system, this time mounted on a UAV via a gimbal system (Photohigher, Wellington, New Zealand) for simultaneous stabilization of both the upwards and downwards view directions. The UAV was based around a Gryphon Dynamics frame and Pixhawk autopilot. The UAV flew over each plot at a similar height as the lift platform, resulting in comparable footprints. The UAV hovered above each plot for approximately 1 min where it collected batches of 25 measurements, bookended by dark current measurements, which were subsequently averaged. Integration times of the QE pro spectrometer measurements were between 0.19 and 0.25 s and 0.34–0.36 s for the upwelling and downwelling channels, respectively. A GoPro camera was mounted in nadir position in the gimbal and used during quality control to make sure the UAV was appropriately positioned above the plot center. The bare soil plot (Fig. 1) provided a zero SIF target to validate our retrievals.

In addition to the PD, the UAV was equipped with two Sony A7R II digital cameras having a Sony FE 35 mm f/2.8 ZA Carl Zeiss Sonnar T* lens and an Applanix APX-15-EI UAV direct georeferencing system. The cameras were tilted in the flight direction to 15° oblique angles from the vertical to enable detailed 3D object reconstruction. For this purpose, the UAV was flown at a height of 50 m which yielded a ground spatial resolution of 0.64 cm. The flight time was 11:22–11:50 AM. The data was gathered using a double grid pattern consisting of 6 north to south and 9 east to west flight lines, ensuring a minimum of 9 overlapping images covering the whole experimental area. The dataset was subsequently used to retrieve dense point clouds with point densities of 2.26–2.43 points/cm using the Agisoft PhotoScan Professional commercial software (AgiSoft LLC, St. Petersburg, Russia). The details of the photogrammetric processing protocol are described by Viljanen et al. (2018).

2.2.2. SIF processing and retrieval

Spectral data were converted from digital numbers to calibrated radiometric values using laboratory calibration coefficients processed with custom Matlab scripts (The Mathworks Inc., Natick, Massachusetts). The scripts and data are available online at https://doi.org/10.5281/zenodo.4607784. There was a small offset in the spectral sampling locations of the upwelling and downwelling calibrated radiances which we estimated as 0.03 nm at the O_2-A feature. We corrected this offset using an interpolation-based technique which is described in Atherton et al. (2019) where the smoothing parameter value was set to 0.99. TOC SIF in the two oxygen absorption bands (i.e., O_2–A and O_2–B) located at 760.77 nm and 687.12 nm were retrieved using Spectral Fitting Methods (SFM) with the spectral ranges of 685.93–691.17 nm and 756.57–768.84 nm for O_2–B and O_2–A, respectively (Meroni et al., 2010). Linear and quadratic polynomials were used to represent the shapes of the fluorescence and reflectance curves, respectively. SIF from these two bands is expressed as F_{687} and F_{760} hereafter.

2.3. Leaf level measurements

2.3.1. PAM measurements

A Pulse-Amplitude-Modulated PAM-2500 (Heinz Walz GmbH, Effeltrich, Germany) was used to measure instantaneous steady state fluorescence (F_t) and maximum fluorescence (F_m') values of fully developed leaves from the sun exposed top canopy ($N = 10$ replicates per plot). A saturating pulse of 800 ms and c. 8000 μmol PAR was used to reach the maximal fluorescence level. These measurements were conducted in sync with the UAV or lift spectral measurements (within 5 min after TOC SIF was measured). The Photosystem II (PSII) operating efficiency Φ_P was estimated as:

$$\Phi_P = \frac{F_m' - F_t}{F_m'} \tag{4}$$

Additionally, NPQ was also estimated as:

$$\mathrm{NPQ} = \frac{F_{MR} - F_m'}{F_m'} \tag{5}$$

where F_{mR} is the reference maximal fluorescence estimated in the absence of regulatory non-photochemical thermal dissipation or NPQ (Appendix C). In addition we measured the maximum quantum yield of photochemistry, or F_v/F_m, in top canopy leaves by dark adapting the leaves for at least 30 min using dark acclimation clips ($N = 3$ replicates per plot), where $F_v = F_m - F_o$, and F_o and F_m are minimal and maximal fluorescence signal as measured with PAM fluorometry in the dark, respectively.

2.3.2. Leaf fluorescence yield estimation

Although PAM fluorescence dynamics are proportional to the variation in fluorescence yield at the level of photosystem II (Φ_{F_PSII}) they do not provide a direct measure of it. First, PAM fluorescence includes also a significant fluorescence contribution from chlorophyll *a* molecules associated to photosystem I (PSI) (especially in the far-red bands as measured with most PAM fluorometers). Second, absolute PAM fluorescence levels (typically in arbitrary units or mV) will also depend on fluorometer settings and sample properties which complicate the estimation of fluorescence yield at the level of PSII Φ_{F_PSII}. Fortunately, PAM fluorescence levels can be corrected for PSI fluorescence, normalized and benchmarked to a theoretical value to facilitate the estimation of separated Φ_{F_PSII} and Φ_{F_PSI} (fluorescence yield at the level of PSI). This method is fully described in Appendix C.

2.3.3. Leaf stomatal conductance and photosynthesis

Photosynthetic gas exchange measurements conducted with a portable IRGA are time consuming. Accordingly, because we were interested in following a large number of leaves within a small period of time and in sync with lift SIF measurements, we measured instead leaf stomatal conductance (g_s) with a leaf porometer (AP4 Porometer, Delta-T Devices, Cambridge, U.K.) from 10 randomly selected fully developed top canopy leaves. Additionally, light responses and A-C_i curves were conducted separately in three replicates across control and treatment

plots using a Walz GFS-3000 portable IRGA (Heinz Walz GmbH, Effeltrich, Germany). From these data, net photosynthesis (A) was estimated based on Ball-Berry model (Ball et al., 1987) as:

$$g_s = m \times \frac{A \times RH}{Cs} + g_0 \quad (6)$$

where RH is relative humidity, Cs is CO_2 concentration at the leaf surface, m is the slope of the relationship between g_s and A×RH/ Cs (the Ball-index), and g_0 is the residual stomatal conductance when A approaches zero, here we set g_0 as 0 as the original Ball-Berry model (Ball et al., 1987). The slope m was estimated using gas exchange measurements of GFS-3000. To estimate actual A, we assumed Cs as air CO_2 concentration (415 ppm), RH was measured from a nearby weather station (SMEAR III, Helsinki) located approximately 3.9 km away from the experiment site, and g_s corresponded to the leaf porometer measurements. GPP was then estimated as:

$$GPP = A + R_d = \frac{g_s \times Cs}{m \times RH} + R_d \quad (7)$$

where R_d is daytime respiration, assumed here to correspond with the rate of CO_2 measured with the IRGA at zero PAR and similar temperature, for simplicity. However, this assumption may result in slight overestimation of GPP due to the Kok effect (Sharp et al., 1984), but we assume this will affect equally all plots. These stomatal conductance-based estimates of GPP were acquired during the diurnal cycles and across experimental plots and used to investigate the effect of Φ_{F_PSII} and LAD on the relationship between SIF and GPP during water stress (objective 3).

2.3.4. Leaf spectral and biochemical measurements

Fully-developed and top canopy leaves were randomly sampled across three separate plants ($N = 3$ replicates per plot) in each of the plots during the morning of the 16 July and used for spectral and biochemical analysis. Leaf directional-hemispherical reflectance (R) and transmittance (T) factors (325–1000 nm) were measured indoors using freshly cut leaves kept in water. Then leaf absorption (Abs) were estimated as integration of $1 - R - T$ over 400–700 nm. The setup consisted of an ASD Hand-Held Spectroradiometer (ASD Inc., Boulder, CO, USA) with spectral sampling of 1.6 nm and FWHM of 3.5 nm connected to an RTS-3ZC Integrating Sphere (ASD Inc., Boulder, CO, USA) through an optical fiber.

Chlorophyll a and b contents (C_{ab}) were estimated from leaf samples collected across the same plants as the spectral measurements. Five circular pieces were cut from each leaf in situ using a cork borer, pooled together into a cryotube and immediately frozen in liquid nitrogen using a portable dewar (CX-100, Taylor Wharton International LLC, Minnetonka, MN). When taken out of the cryotubes, the samples were extracted in an oven at 50 °C for four hours, after which, Chlorophyll a and b extraction and estimation were conducted after Wellburn (Wellburn, 1994), using dimethyl sulfoxide (DMSO) and analyzed using a Shimadzu UV-1800 spectrometer (Shimadzu Corporation, Kyoto, Japan). Leaf spectral measurements were used for Fluspect model inversion (see Appendix D). Leaf chlorophyll contents were used to validate the inversion of C_{ab} (Fig. D1 in Appendix D).

2.4. Canopy and structural measurements

2.4.1. LAI and canopy temperature

LAI was estimated using the pin-point method (Jonasson, 1988; Mänd et al., 2010). Firstly, we drew a line diagonally across the plots and marked sampling nodes at 50 cm intervals. These marks produced 14 randomly distributed points across the plot. Next we counted the number of leaves that intercepted with a sharp pin weight vertically hanging from the diagonal line at every node as it descended through the canopy. This number corresponds with a direct measurement of LAI at that particular point (ranging from 0 for points between rows, to up to 4 for points directly over a potato plant). The canopy LAI was estimated as the average of all readings. It is important to note however that this method provides only a measure of directional effective LAI and will tend to underestimate total projected LAI (as in SCOPE).

An Infrared camera (Optris P450, Optris GmbH, Germany) mounted adjacent to the PD system was used to register diurnal patterns in canopy temperature every two minutes during spectral data collection. The average temperature within the estimated Piccolo fiber footprint was used as canopy temperature.

2.4.2. Leaf angular distribution estimation

We used two methods to estimate LAD. Firstly, we used a ground-based photographic method (Pisek et al., 2011) for collection of diurnal-temporal datasets of LAD variation in W7 and W8. In addition, we developed a new method to estimate LAD from the photogrammetrically derived point clouds using UAV image data for spatial datasets (Xu et al., 2020).

The photographic method was used to estimate leaf inclination angle during diurnal measurements in control and treatment plots. Photographs were taken with a cell phone camera (Honor 9, Huawei Technology Co., Ltd., Shenzhen, PRC) fixed on a tripod perpendicular to the ground. The cell phone was placed outside the plots at a distance approximately 50 cm from the plot edge. We took repeated photographs of three potato sections in sync (within 5 min) with lift level measurements of SIF every 1 h. The leaf inclination angle was determined from photographs using the ImageJ software (http://rsb.info.nih.gov/ij/) following the standard approach (Pisek et al., 2011). Average leaf inclination angle (ALA) from 3 pictures in a total of 12 leaves were estimated at each time-point. For diurnal LAD estimation, we use a two-parameter leaf inclination distribution function to model LAD. We used ALA to estimate the parameter LIDFa as (Verhoef, 1998):

$$\mathrm{LIDFa} = \frac{(45^\circ - \mathrm{ALA}) \times \pi^2}{360} \quad (8)$$

Another parameter LIDFb was fitted from Verhoef's leaf angle algorithm combining LAD estimated from dense point clouds data (see below description), and was assumed as constant during diurnal measurements. We estimated LAD using these two parameters: LIDFa and LIDFb through Verhoef's leaf angle algorithm, which links ALA to LAD.

A UAV based Structure from Motion (SfM) photogrammetric method was used to obtain LAD directly (i.e. without application of Eq. 8) for each of the 10 plots in the spatial analysis. The method and equations are fully described in Xu et al. (2020). In brief, before retrieving LAD, first we classified leaf and soil according to point height by setting a threshold value which was plot dependent. Then, and referring to Xu et al. (2020), we used the Agisoft normal vectors directly, rather than the SVD method, as we found that the SVD method produced unreliable results for leaves demonstrating extreme wilting angles. Finally, the SfM method returned a small proportion of zenith angles greater than 90° (Fig. B1), which is outside the SCOPE defined inclination angle range of 0–90°. In these cases, the negative of the leaf normal vector was used as a substitute in SCOPE modelling e.g. 92° was replaced with 88°.

2.5. Investigating the relative role of LAD and Φ_F of TOC SIF with radiative transfer simulations

We conducted a SCOPE (v1.73) scenario-based sensitivity analysis to disentangle the causes of SIF variation (Fig. 2) (see Appendix D for details on SCOPE implementation). The analysis focused on the variables that we hypothesized to control SIF variation across the diurnal and spatial domains: Φ_{F_PSII} and LAD. The analysis was structured to address our 3 objectives (see Table 1 for a summary): quantify the relative role of Φ_{F_PSII} and LAD in 1) the diurnal and 2) spatial variation in TOC SIF; as well as 3) the relationship between SIF and GPP. Several model scenarios were generated by either keeping Φ_{F_PSII} and LAD fixed to a

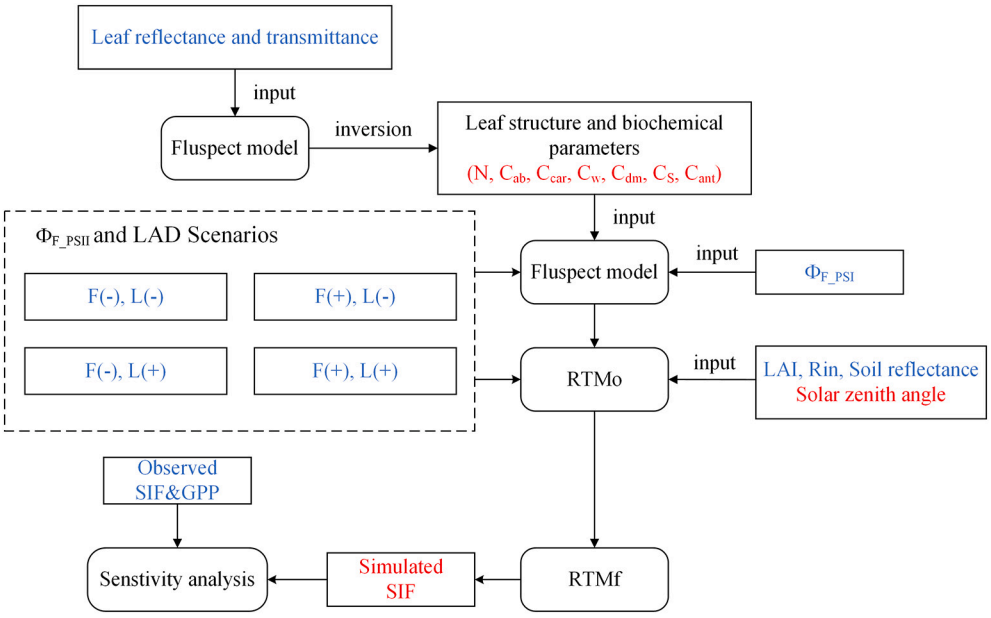

Fig. 2. Flow diagram used for the simulation of TOC SIF scenarios based on combinations between fixed (−) and dynamic (+) Φ_{F_PSII} (F) and LAD (L). The results from these scenarios were used to estimate the relative role of Φ_F and LAD on the diurnal and between-plot-pairs spatial dynamics of TOC SIF. Measured variables are displayed in blue, simulated variables in red. RTMo and RTMf are two submodules of SCOPE. See section 2.5 text for details. (For interpretation of the references to color in this figure legend, the reader is referred to the web version of this article.)

Table 1
SCOPE scenario simulations and their relation to the objectives.

Objective	Scenario	Φ_{F_PSII}	LAD	Designation
Objectives 1 and 3: Role of Φ_{F_PSII} and LAD on the diurnal response to water stress; and diurnal/ spatial coupling between SIF:GPP	s1	Fixed	Fixed	F(−), L(−)
	s2	Fixed	Dynamic	F (−), L(+)
	s3	Dynamic	Fixed	F (+), L(−)
	s4	Dynamic	Dynamic	F (+), L(+)
Objective 2: Role of Φ_{F_PSII} and LAD on the spatial response to water stress (see Fig. 3)	s5	Control	Control	F (c), L(c)
	s6	Control	Treatment	F (c), L(t)
	s7	Treatment	Control	F (t), L(c)
	s8	Treatment	Treatment	F (t), L(t)
	s9	Control	Control	F (c), L(c)

reference value or allowing them to follow the measured dynamics. SIF differences between scenarios were used to calculated sensitivity indices which quantified the relative influence of Φ_{F_PSII} or LAD on diurnal and spatial (between treatment pairs) SIF variation. Scenario output was also used to explore the correlation between SIF and GPP as a function of varying Φ_{F_PSII} or LAD.

Sensitivity indices, S, were calculated from absolute differences (ΔSIF) in SIF scenario values. For brevity, we refer to Φ_{F_PSII} and LAD as F and L respectively, and scenarios are characterized by the binary state of L and F which is either dynamic (in time or space) or fixed. We used two sets of scenarios to generate ΔSIF which each have corresponding binary states. The first set of scenarios (s1-s4) were used to evaluate the role of F and L in driving diurnal SIF (Objective 1) and their impact on the SIF: GPP relationship both over the diurnal and spatial scales (Objective 3). The scenarios separated the diurnal variation in SIF from that driven by changing PAR alone, which we labelled as $APAR_{SUN}$. Variability of F and L are denoted with symbol + and constancy with symbol −. For diurnal analysis, fixed values corresponded to first point observations in the morning. For the spatial analysis fixed F and L values corresponded to the maximum F and minimum average leaf angle (ALA) registered across plots. As an example, in scenario 3 we vary Φ_{F_PSII} diurnally and keep LAD fixed, hence this scenario is denoted as: $s3 : F(+), L(-)$ and the SIF difference between this scenario and baseline scenario s1 where both Φ_{F_PSII} and LAD are fixed, i.e. the scenario in which SIF is driven by $APAR_{SUN}$, is:

$$\Delta SIF(\Phi_{F\_PSII}) = |SIF(s1 : F(-), L(-)) - SIF(s3 : F(+), L(-))| \quad (9)$$

In the second set of scenarios (s5-s9, see Table 1 and Fig. 3), the difference in SIF between pairs of control (c) and treatment (t) was analyzed. In these scenarios difference between control and treatment plots were analyzed diurnally using data from plot W7 and W8, and spatially using data across all paired plots. An equivalent to Eq. (9) to denote the change in SIF due to Φ_{F_PSII} in these scenarios is

$$\Delta SIF(\Phi_{F\_PSII}) = |SIF(s5 : F(c), L(c)) - SIF(s7 : F(t), L(c))| \quad (10)$$

Given the described notation and returning to the first set of scenarios (s1-s4), then the sensitivity index characterizing the relative influence of Φ_{F_PSII} on diurnal variation in SIF over and above $APAR_{SUN}$ was calculated as:

$$S_F^d = \frac{\Delta SIF(\Phi_{F\_PSII})}{\Delta SIF(\Phi_{F\_PSII}) + \Delta SIF(LAD)} = \frac{|SIF(s1 : F(-), L(-)) - SIF(s3 : F(+), L(-))|}{|SIF(s1 : F(-), L(-)) - SIF(s4 : F(+), L(+))|} \quad (11)$$

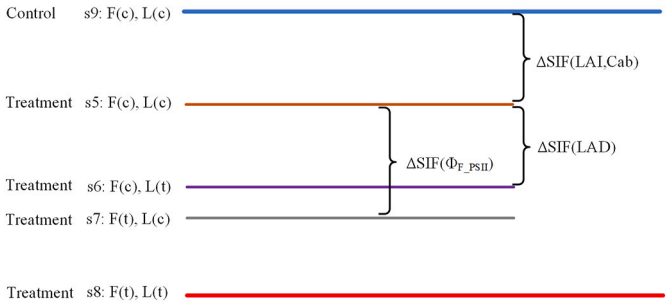

Fig. 3. Graphic representation exemplifying the estimation of the relative role of factors controlling the spatial variation in TOC SIF between treatment (t) and control (c) plot-pairs, using SCOPE simulated scenarios (s) with diverging values for Φ_{F_PSII} (F) and LAD (L). Scenarios s5-s8 correspond to treatment plots, in which symbol 't' indicates that the value originated from the very same treatment plot, and symbol 'c' indicated that the value was taken from the control plot paired to that treatment. For example, in scenario s5 we use the F and L values recorded in the control plot to simulate treatment plot SIF, hence the SIF difference between this scenario and baseline scenario s9 control SIF, reflects the impact of factors other than F and L, namely LAI and C_{ab} ΔSIF (LAI, C_{ab}).

Similar to Eq. (11), the sensitivity index characterizing the relative influence of LAD on diurnal variation in SIF relative to $APAR_{SUN}$ was calculated as.

$$S_L^d = \frac{\Delta SIF(LAD)}{\Delta SIF(\Phi_{F\_PSII}) + \Delta SIF(LAD)} = \frac{|SIF(s1: F(-), L(-)) - SIF(s2: F(-), L(+))|}{|SIF(s1: F(-), L(-)) - SIF(s4: F(+), L(+))|} \quad (12)$$

The diurnal sensitivity indices, S_F^d and S_L^d, were calculated for both treatment and control plots W7 and W8 to investigate the comparative influence of Φ_{F_PSII} and LAD during water treatment and control conditions relative to the baseline state of $APAR_{SUN}$.

In the second set of scenarios (s5-s9), which characterize the difference in SIF between control and treatment plots, the control scenario replaces the baseline $APAR_{SUN}$ scenario used in Eq. (11) and (12) (Fig. 3). In s5-s9, there was an additional source of variation that must be considered. That is variation in LAI and C_{ab}. The sensitivity index characterizing the relative influence of Φ_{F_PSII} on variation in SIF was calculated as:

$$S_F^{c:t} = \frac{\Delta SIF(\Phi_{F\_PSII})}{\Delta SIF(\Phi_{F\_PSII}) + \Delta SIF(LAD) + \Delta SIF(LAI, Cab)} = \frac{|SIF(s5: F(c), L(c)) - SIF(s7: F(t), L(c))|}{|SIF(s9: F(c), L(c)) - SIF(s8: F(t), L(t))|} \quad (13)$$

Similarly, the sensitivity index characterizing the relative influence of LAD on spatial variation in SIF was calculated as:

$$S_L^{c:t} = \frac{\Delta SIF(\mathrm{LAD})}{\Delta SIF(\Phi_{F\_PSII}) + \Delta SIF(LAD) + \Delta SIF(LAI, Cab)} = \frac{|SIF(s5: F(c), L(c)) - SIF(s6: F(c), L(t))|}{|SIF(s9: F(c), L(c)) - SIF(s8: F(t), L(t))|} \quad (14)$$

The above two indices were applied to plot differences in diurnal (W7, W8) and pair-wise spatial plots (W1-W10). The difference being that in the diurnal case the influence of LAI and C_{ab} was constant through time, whereas these values varied in the spatial case.

The dynamics of LAD can impact SIF via two main mechanisms. These two mechanisms are LAD induced changes in APAR, which we denote at $APAR_{LAD}$, and LAD induced changes in escape probability, f_{esc}^{LAD}. To separate SIF variability between these two mechanisms we use an additional output, total SIF emitted at photosystem level (SIF_{total}), where the ratio between TOC SIF and SIF_{total} is the SIF escape probability, f_{esc}. We then combine SIF_{total} and f_{esc} output from multiple scenarios to separate between $APAR_{LAD}$ and f_{esc}^{LAD} mechanisms. As such, the following sensitivity index is used to assess $APAR_{LAD}$ influence between control and treatment plots:

$$S_{L:APAR}^{c:t} = \frac{\Delta SIF(LAD:APAR)}{\Delta SIF(LAD)} = \frac{|SIF(s5: F(c), L(c)) - SIF_{total}(s6: F(c), L(t)) \times f_{esc}(s5: F(c), L(c))|}{|SIF(s5: F(c), L(c)) - SIF(s6: F(c), L(t))|} \quad (15)$$

And the following index to assess the influence of LAD induced variation in f_{esc}^{LAD} on SIF between control and treatment plots:

$$S_{L:f_{esc}}^{c:t} = \frac{\Delta SIF(LAD: f_{esc})}{\Delta SIF(LAD)} = \frac{|SIF(s5: F(c), L(c)) - SIF_{total}(s5: F(c), L(c)) \times f_{esc}(s6: F(c), L(t))|}{|SIF(s5: F(c), L(c)) - SIF(s6: F(c), L(t))|} \quad (16)$$

The relative contributions of $APAR_{LAD}$ and f_{esc}^{LAD} were also assessed for diurnal data over and above the $APAR_{SUN}$ baseline where scenarios s5, s6 were substituted with s1 and s2 to calculate the indices $S_{L:APAR}^d$ and $S_{L:fesc}^d$.

SIF scenario predictions were validated against the lift platform observations in the diurnal domain, and UAV observations in the spatial domain. When validating model performance, we compared diurnal trends in observed SIF to simulated SIF using normalized (relative) values, due to a bias error between simulated and observed data (simulated SIF have higher value, see Figs. B2 and B3). This bias and differences are expanded on in the discussion. Relative diurnal patterns of SIF were calculated by normalizing SIF data using the first value in the morning for the observed and simulated to evaluate simulation performance by comparing their variation trends. Under validation, we expected those scenarios where all variation was accounted for, e.g. scenario 4 in the diurnal and spatial domain, to have the highest R^2 when compared to observations. As a final note, Eq. (11–16) assumes linear superposition of individual variables. There were small errors due to the violation of this assumption. For example, the interaction between variables results in errors of 5% in the diurnal variation characterization and 0.5% in the spatial characterization. As the errors were relatively small, we did not analyze these higher order interactions further.

2.6. Estimation of the fluorescence escape probability, f_{esc}

The relationship between GPP and SIF depends on the fluorescence escape probability, f_{esc}, which itself depends on the LAD. Therefore, and in addition to the sensitivity analysis outlined above, we estimated f_{esc} at 760 nm using observations of NIRv and FCVI and the approach described by Zeng and Yang (Yang et al., 2020; Zeng et al., 2019). The estimation of f_{esc} via NIRv and FCVI, requires fPAR. Here, we use Rededge_NDVI as a proxy of fPAR using Eq. (17) and (18) (Miao et al., 2018; Viña and Gitelson, 2005):

$$\mathrm{Rededge\_NDVI} = \frac{R_{750} - R_{705}}{R_{750} + R_{705}} \quad (17)$$

$$fPAR = 1.37 \times \mathrm{Rededge\_NDVI} - 0.17 \quad (18)$$

where R_{750} and R_{705} are canopy reflectance at 750 nm and 705 nm. Then, f_{esc} based on NIRv and FCVI can be estimated using $\frac{NIRv}{fPAR}$ and $\frac{FCVI}{fPAR}$, respectively. In addition, fPAR was used to normalize SIF, prior to comparison with the leaf-based GPP estimates.

We also calculated f_{esc} from our model simulation using Eq. (19):

$$f_{esc} = \frac{\pi \times SIF_{obs}}{SIF_{total}} \quad (19)$$

where, SIF_{obs} is observed TOC SIF, and SIF_{total} is total SIF at photosystem level.

3. Results

3.1. Spatial and diurnal response of photosynthetic and canopy structural parameters to water stress

Differences in photosynthetic and canopy structural parameters were observed between control and treatment plots in response to the water stress treatment (Fig. 4). As expected, photosynthetic parameters Φ_P, Φ_{F_PSII}, F_v/F_m, and estimated GPP tended to be higher in control relative to treatment plots. UAV retrieved SIF, F_{760}, was also higher in control plots. Interestingly, total chlorophyll (C_{ab}) contents in top leaves were higher in the treatment plots than in the controls. In terms of structural responses, LAI was increased in control plots relative to treatment plots and, as expected, the ALA of the controls was lower than in the treatment plots.

The diurnal time series of canopy mean temperature, g_s, NPQ, Φ_P, Φ_{F_PSII}, and ALA for plots W7(c) and W8(t) is reported in Fig. 5. Due to a temporary failure in the lift platform, measurements for the control plot stopped at 16:30. However, clear temporal patterns could be observed in both treatment and control plots. Canopy mean temperature, ALA and NPQ increased during the morning and gradually decreased or remained

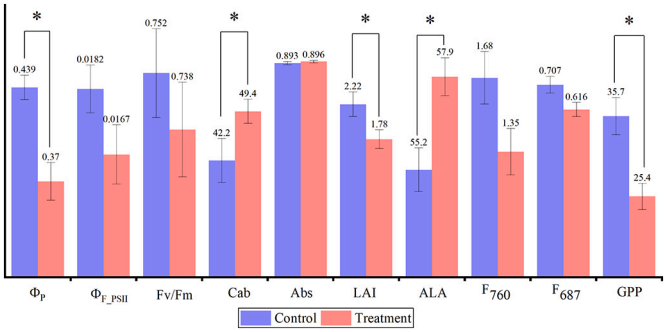

Fig. 4. Values of key variables in control and treatment plots (Mean ± SE, $N = 5$) measured around noon two weeks after removal of irrigation. From left to right: operating quantum yield of photochemistry Φ_P, quantum yield of fluorescence in PSII Φ_{F_PSII}, maximum quantum yield of PSII photochemistry F_v/F_m, leaf total chlorophyll (C_{ab}) ($\mu g\ cm^{-2}$), leaf PAR absorption Abs, leaf area index (LAI), average leaf angle (ALA) (degrees), UAV F_{760} ($W\ m^{-2}\ \mu m^{-1}\ sr^{-1}$), UAV F_{687} ($W\ m^{-2}\ \mu m^{-1}\ sr^{-1}$) and GPP ($\mu mol\ m^{-2}\ s^{-1}$). Asterisks means the parameters are significantly different using the Kruskall-Wallis test ($p < 0.05$). All leaf level variables were measured in top canopy leaves.

high during the afternoon. In treatment and control plots, Φ_{F_PSII} and Φ_P show similar patterns with a decreasing trend for most of the day, followed by a smaller increase in the late afternoon. Consistent with the spatial data, treatment plots showed higher values in ALA and NPQ, and g_s, Φ_P and Φ_{F_PSII} were reduced compared with control plots.

3.2. Sensitivity of diurnal SIF variation to LAD and Φ_{F_PSII}

Diurnal patterns of measured and simulated SIF are shown in Fig. 6. To facilitate the visual comparison of patterns between measurements and simulations, data were normalized by first time series values; results without normalization are shown in Fig. B2. Simulations accounting for variation in both LAD and Φ_{F_PSII} (F(+), L(+)) tended to better reproduce the diurnal pattern of observed SIF compared to scenarios where only LAD (F(−), L(+)), Φ_{F_PSII} ((F(+), L(−)) or neither variable (F(−), L(−)) was allowed to vary (Fig. 6), which tended to overestimate SIF. The only exception was the case of F_{687} in the control plots where (F(+), L(+)) underestimated measured SIF in the afternoon.

Clear differences in the diurnal patterns of relative sensitivity of TOC SIF to LAD and Φ_{F_PSII} were found between control and treatment plots, as shown in Fig. 7. In the control plot, the sensitivity to LAD and Φ_{F_PSII} was relatively constant and equal in magnitude over the course of a day. After accounting for $APAR_{SUN}$ approximately 42%–56% of simulated control plot diurnal F_{760} variation was driven by LAD, and 44%–58% by Φ_{F_PSII}. In contrast, the relative contribution of these two factors was dynamic over the course of the day for the treatment plots. However, it should be kept in mind that Fig. 7 only shows a partial diurnal cycle. This is important as LAD under stress probably adjusted prior to the 10 am

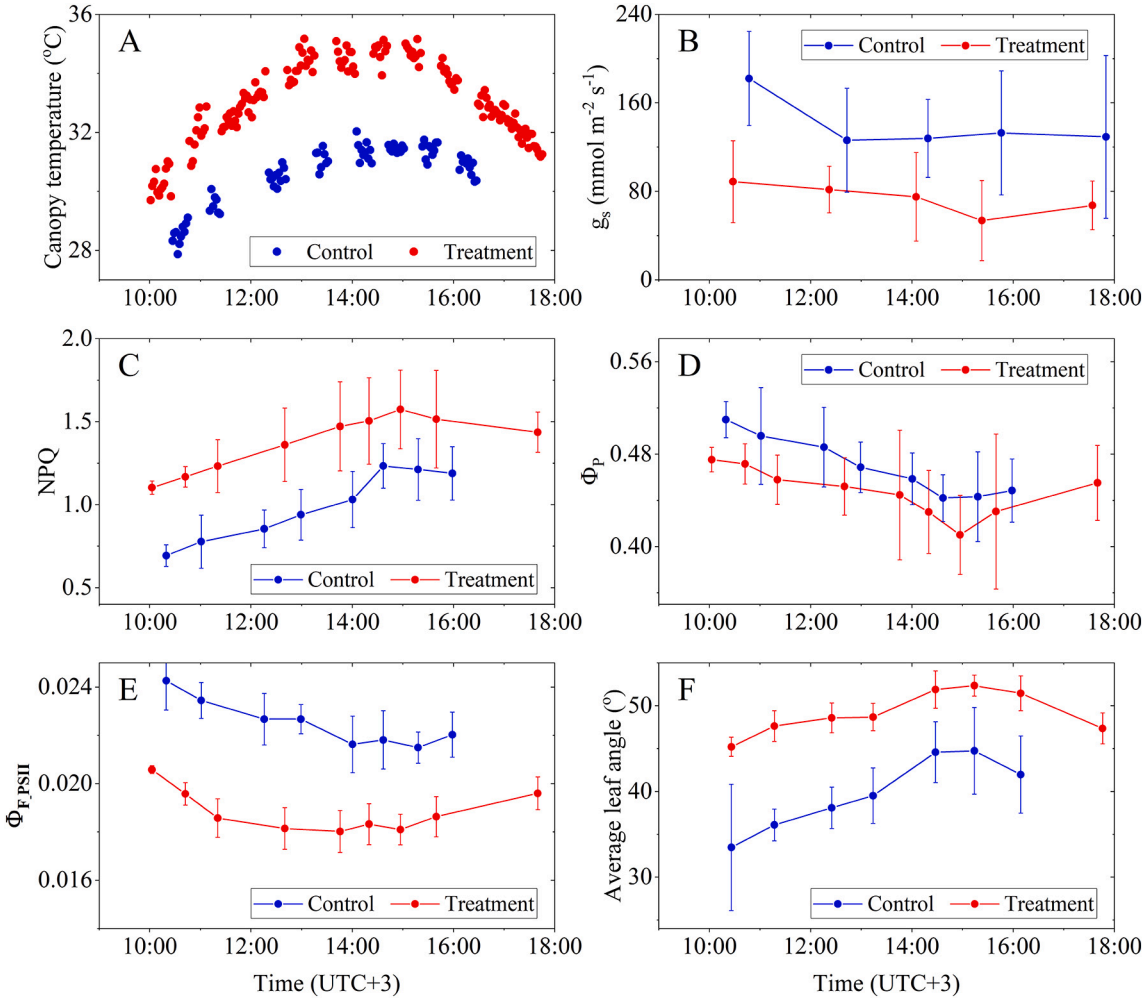

Fig. 5. Diurnal patterns in canopy temperature, photosynthetic and structural variables in potato plants for the control (W7) and treatment (W8) plot pair. From panel A to F, canopy temperature ($^\circ C$), stomatal conductance ($mmol\ m^{-2}s^{-1}$), non-photochemical quenching (NPQ), operating quantum yield of photochemistry Φ_P, quantum yield of fluorescence in PSII Φ_{F_PSII}, and average leaf angle (ALA) (degrees).

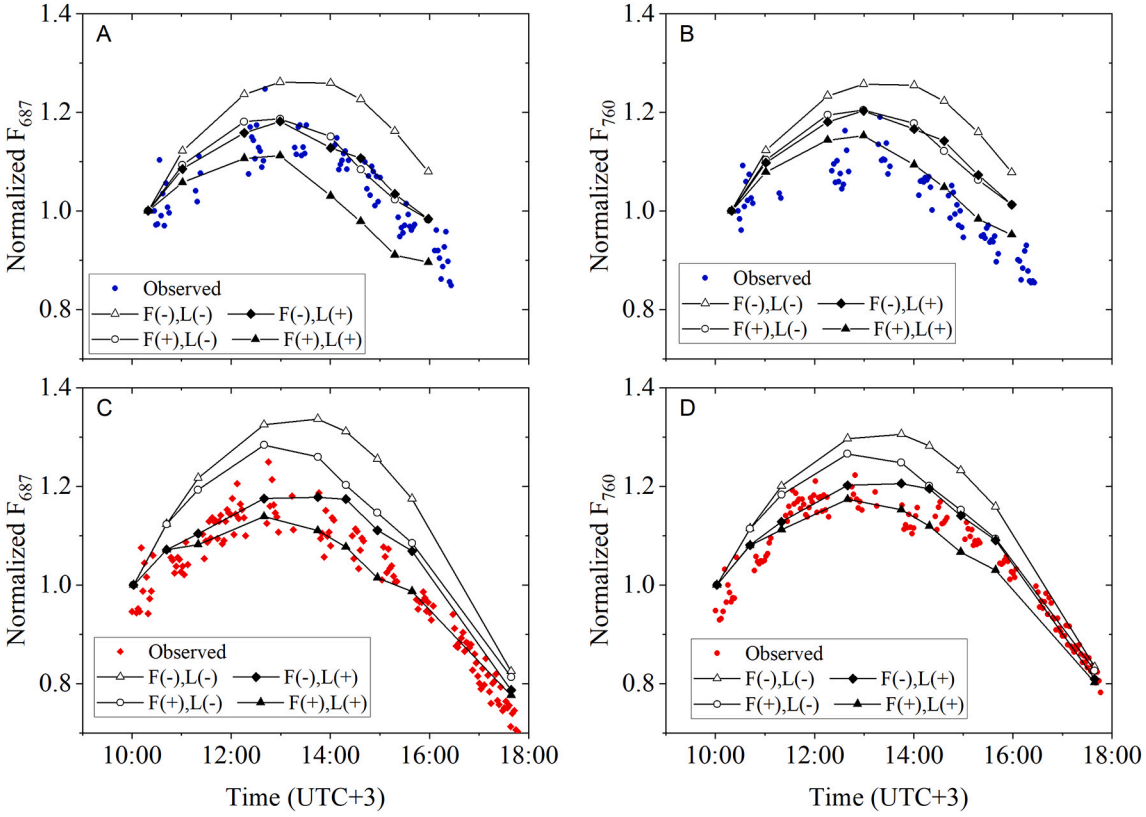

Fig. 6. Diurnal patterns of variation of observed SIF and SCOPE simulated SIF scenarios for the control (panels A-B, W7) and treatment (panels C—D, W8) plot pair. SIF are normalized by first time series values. SIF scenarios (see Table 1 s1-s4) were simulated using either measured dynamic (+) or fixed (−) values for the quantum yield of fluorescence in PSII Φ_{F_PSII} (F) and LAD (L).

start of observations.

3.3. Sensitivity of SIF variation to LAD and Φ_{F_PSII} in control and treatment pairs

Next, we used the sensitivity analysis to evaluate the factors that drove the observed diurnal differences in SIF between the control and treatment pair W7 and W8 (Fig. 8, Table 2). The differences were due to a number of factors including LAI and C_{ab} which impacted APAR ($APAR_{LAI,Cab}$); LAD which impacted both APAR ($APAR_{LAD}$) and f_{esc}; and Φ_{F_PSII}. In F_{760}, $APAR_{LAI,Cab}$ variations between treatment and control plots explained 39% of the differences in SIF. Secondly, about 30%–36% of SIF decrease between treatment and control plots was caused by Φ_{F_PSII}, and LAD variation accounted for 25%–31% of the decrease, distributed as: 3% $APAR_{LAD}$ and 22–28% f_{esc}.

To complement the diurnal sensitivity testing, we also evaluated the spatial drivers of differences in SIF between control and treatment plots at a fixed point in time (Fig. 9). Here we analyzed simulations of F_{760} for five control pair plots. The comparison of simulated and UAV observed F_{760} is shown in Fig. B3 (R^2 = 0.81). A general decrease in F_{760} in response to the water stress could be seen across plot pairs both in observations (ΔF_{760_Obs}) and simulations (ΔF_{760_Mod}). In individual plot-pairs, the model underestimated the decrease by up to 0.23 W m^{-2} μm^{-1} sr^{-1} in W1/W2, and overestimated the difference by up to 0.55 W m^{-2} μm^{-1} sr^{-1} in plot pair W9/W10 (Fig. 9).

The simulation-based sensitivity analysis revealed that the water stress treatment expressed itself in multiple ways depending on the plot pair under consideration. According to the simulations, the background contribution of $APAR_{LAI,Cab}$ explained 20% to 72% of variability between control and treatment plots, mainly determined by differences in LAI. Spatially the Φ_{F_PSII} contribution for F_{760} varies from 10% to 30%. The LAD mediated f_{esc} contribution also changes from 5% to 39%. In short, although SIF consistently decreased in the treatment plots two weeks into the water stress experiment and compared to control plots, the simulated decrease was not attributable to a single driver or mechanism.

3.4. The link between SIF and GPP

To conclude our analyses, we assessed the impact of variation in LAD and Φ_{F_PSII} on the SIF:GPP relationship. Fig. 10 shows relationships between F_{760} normalized by fPAR and leaf level GPP estimated from stomatal conductance across diurnal and spatial scales. We normalized SIF by fPAR, as the GPP measurements were conducted at the leaf level and are therefore free of soil/gaps. In the diurnal analysis, a moderate linear relationship was found between simulated F_{760}/fPAR and GPP, when LAD or Φ_{F_PSII} were set to constant using the first timeseries values. When either LAD or Φ_{F_PSII} was set to observed values, these relationships increased with almost the same slope and R^2 (0.52 and 0.51, respectively) (Fig. 10A). The scenario which considered variation in both LAD and Φ_{F_PSII} had the best performance ($R^2 = 0.61$). In the spatial analysis, similar results were found in the comparison between simulated SIF and GPP. Again, the scenario which accounted for variation in both LAD and Φ_{F_PSII} accounted for the largest fraction of observed variance ($R^2 = 0.68$). The relationships between measured SIF/fPAR and GPP were weaker than the simulated values, with R^2 = 0.36 (Fig. 10B and D) for both diurnal lift and spatial UAV platforms. It is also important to note that we observed a substantial increase in the stomatal conductance measurements between days, which explains the higher GPP levels in the spatial dataset relative to the diurnal. These differences probably related to differences in the calibration of the porometer between the two days and do not affect the comparison of scenarios presented in Fig. 10, but do point to possible inaccuracies in the absolute GPP values.

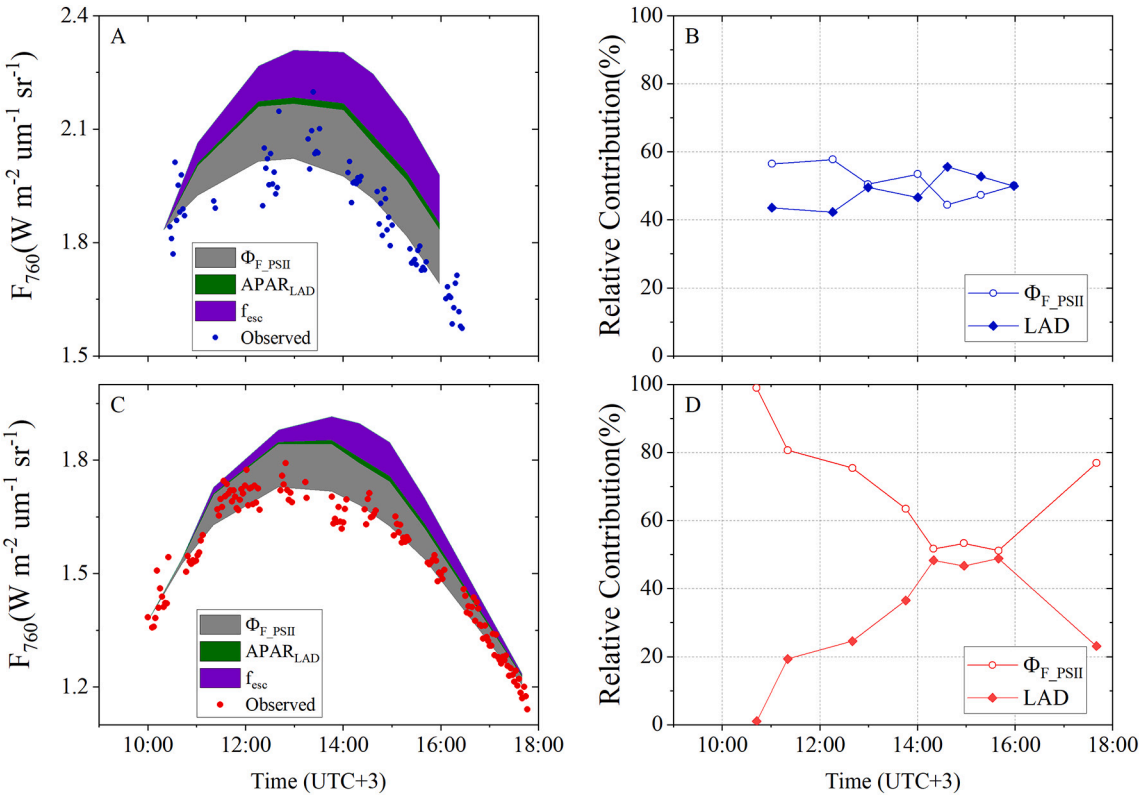

Fig. 7. Sensitivity of diurnal simulated normalized F_{760} to the quantum yield of fluorescence in PSII (Φ_{F_PSII}) and leaf angle distribution (LAD) for the control (W7, panels A-B) and treatment (W8, panels C—D) plot pair. Shaded areas (panels A, C) and relative contributions (B, D) were calculated using simulated data. Measured points provide qualitative validation of the simulated diurnal patterns. Sensitivities were calculated using a baseline scenario of no structural or photosynthetic dynamics ($APAR_{SUN}$). Left two panels display the effect of Φ_{F_PSII} and $APAR_{LAD}$ and f_{esc} in driving SIF change. Right two panels show the relative contribution of Φ_{F_PSII} and LAD to diurnal F_{760} change.

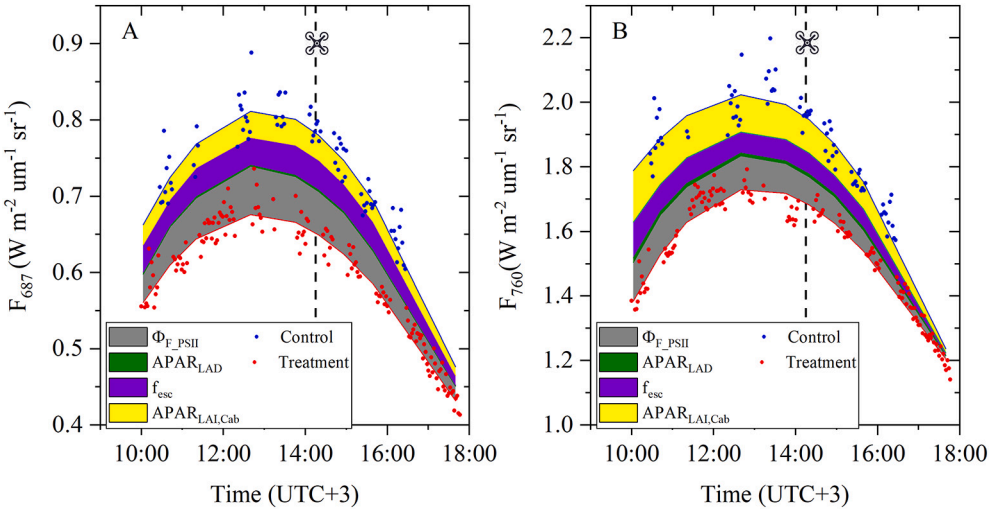

Fig. 8. Diurnal sensitivity of simulated SIF to photosynthetic and structural variables, calculated using the differences between the control (W7) and treatment (W8) plots. F_{687} is shown in panel A and F_{760} in panel B. Variables included changes in canopy light absorption caused by differences in LAI and C_{ab} ($APAR_{LAI,Cab}$) or LAD ($APAR_{LAD}$), as well as differences in the quantum yield of fluorescence in PSII Φ_{F_PSII}, and f_{esc}. The vertical dashed lines marks the time of the UAV spatial measurements, which were carried out on the previous day (see Fig. 9).

4. Discussion

Our aim was to investigate how structural and photosynthetic factors mediate the response of SIF to water stress in a potato crop. Our results showed reductions in SIF, observed using lift and UAV platforms, coincident with the build-up of a stress response that expressed itself across the diurnal and spatial domains, the latter reflecting the expression of water stress two weeks upon the onset of the treatment. Further, the stress manifested itself as photosynthetic and structural variation which simultaneously decreased SIF in water limited plots.

4.1. The role of photosynthetic physiology in SIF variation under water stress

As an isohydric plant, potato is prone to close stomata to prevent excessive water loss and maintain main physiological processes under low soil water potential or water stress conditions, resulting in reduced stomatal conductance (shown in Fig. 5B) (Obidiegwu et al., 2015).

Table 2
Summary of results from SCOPE scenario sensitivity testing across diurnal and spatial domains. The symbology of the Sensitivity Indices is explained in detail in section 2.5. As an example, S_F^d refers to the sensitivity of F_{760} to Φ_{F_PSII} in diurnal simulations, relative to an assumed scenario of no structural or photosynthetic dynamics ($APAR_{SUN}$). Likewise, $S_{L:APAR}^{c:t}$is the variation due to LAD driven APAR of treatment relative to control plots, estimated using spatial simulations. This index was also calculated using temporal simulations, denoted as $S_{L:APAR}^{c:t,\ d}$.

Sensitivity Index	F_{760} variance explained (%)	Figure reference
S_F^d	44%–98%	Fig. 7
S_L^d	2%–56%	Fig. 7
$S_{L:APAR}^d$	5%	Fig. 7
$S_{L:f_{esc}}{}^d$	37%–51%	Fig. 7
$S_F^{c:t,\ d}$	30%–36%	Fig. 8
$S_L^{c:t,\ d}$	25%–31%	Fig. 8
$S_{L:APAR}^{c:t,\ d}$	3%	Fig. 8
$S_{L:f_{esc}}{}^{c:t,\ d}$	22%–28%	Fig. 8
$S_{L:APAR}^{c:t}$	1%–11%	Fig. 9
$S_{L:f_{esc}}{}^{c:t}$	5%–39%	Fig. 9
$S_F^{c:t}$	10%–30%	Fig. 9
$S_L^{c:t}$	6%–50%	Fig. 9

Stomatal closure leads to a decrease in evaporative cooling and a following increase in leaf temperature due to reduction in transpiration rates (Reynolds-Henne et al., 2010), which we observed using infrared imagery shown in Fig. 5A. Stomatal closure also results in a decrease of the intercellular CO_2 concentration (Farquhar et al., 1980), which not only reduces the rate of photosynthetic carbon fixation (decreasing LUE and, via increase in NPQ, decreasing also the fluorescence yield) but, for C_3 plants, will also affect the partitioning between carboxylation/oxygenation of Rubisco in favor of photorespiration (Flexas et al., 2000), further decreasing LUE but, this time, without any direct effect on the fluorescence yield. As a result, despite evidence that stomatal closure induced by water stress has been repeatedly associated with a decrease in fluorescence yields (Cendrero-Mateo et al., 2015; Flexas et al., 2002; Flexas et al., 2000), and consistent also with our results (Fig. 4 and Fig. 5F), the decrease Φ_F should not be linearly related to that of LUE during water stress. This is due to the action of alternative energy sinks such as photorespiration, which affect the slope LUE/Φ_F in Eq. (3) and add non-linearity to relationship between GPP and SIF in response to water stress (Flexas et al., 2002; Helm et al., 2020).

The relationships are further complicated at the canopy level where the slope between SIF and GPP is not only affected by photosynthetic factors (i.e. LUE/Φ_F) but also by structural dynamics ($1/f_{esc}$). We found clear water stress driven reductions in SIF, which were coincident with observed reductions in Φ_F, but also changes in canopy structural parameters (Fig. B6). Over the short term, reflected here by the diurnal response to water stress, our observations suggest that both Φ_F and structural parameters adjust in response to environmental stress (Fig. 5 D, F). Our simulation results suggest that, after accounting for changes in absorbed PAR driven by sun angle ($APAR_{SUN}$), LAD and Φ_F dynamics are of similar importance in determining the diurnal response of SIF to water stress (Fig. 7 and Fig. B7). We speculate that multiple factors combine to determine the remotely sensed drought response of SIF. The structural factors in particular depend on the scale of the observation, which may go some way to explaining the discrepancy between the recent experimental results (Helm et al., 2020; Marrs et al., 2020) and satellite remote sensing observations (Magney et al., 2020; Sun et al., 2015).

We expected the long-term response to water stress, which was investigated two weeks after the onset of water exclusion using spatial data and simulations, to entail changes in canopy structural and photosynthetic properties. Accordingly, we found differences in LAI,

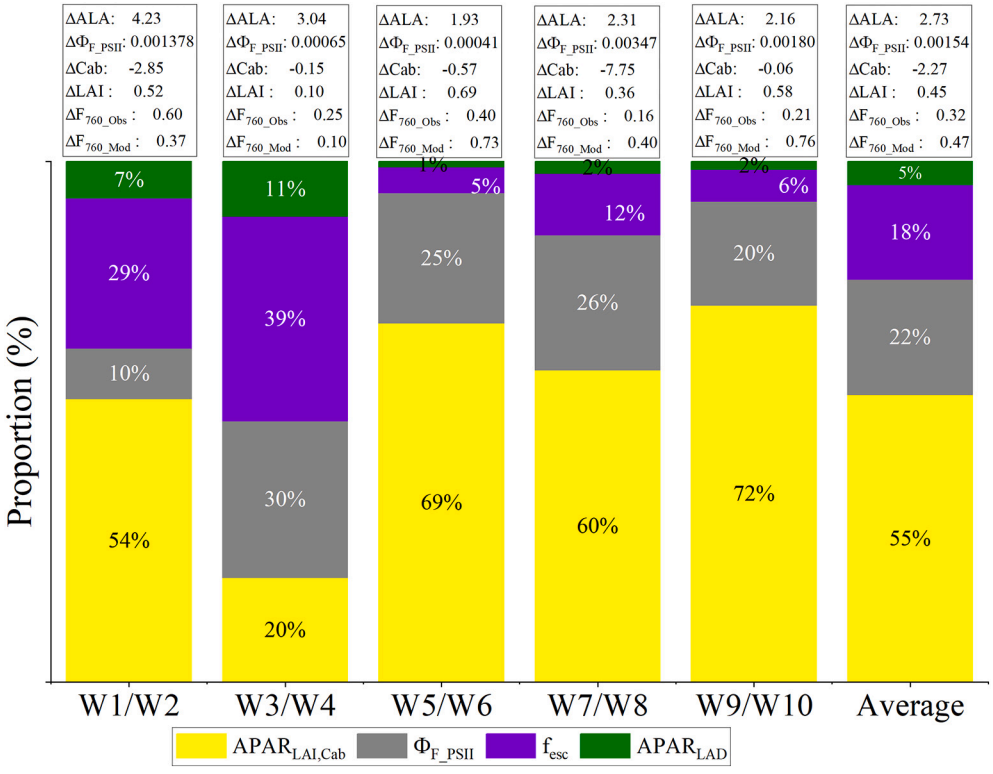

Fig. 9. Spatial sensitivity of simulated SIF (F_{760}) to photosynthetic and structural variables, calculated using the differences between the control and treatment plots. The solid color blocks represent proportions of explained variation between treatment and control pairs. Differences in key variables between control and treatment plot pairs ($\Delta = c - t$) are shown in the top blocks for average leaf angle (ΔALA, degrees), quantum yield of fluorescence in PSII ($\Delta\Phi_{F\_PSII}$), top canopy leaf chlorophyll contents (ΔC_{ab}, $\mu g\ cm^{-2}$), and leaf area index (ΔLAI, $m^2\ m^{-2}$) as well as observed (ΔF_{760_Obs}, $W\ m^{-2}\ \mu m^{-1}\ sr^{-1}$) and modelled F_{760} (ΔF_{760_Mod}, $W\ m^{-2}\ \mu m^{-1}\ sr^{-1}$).

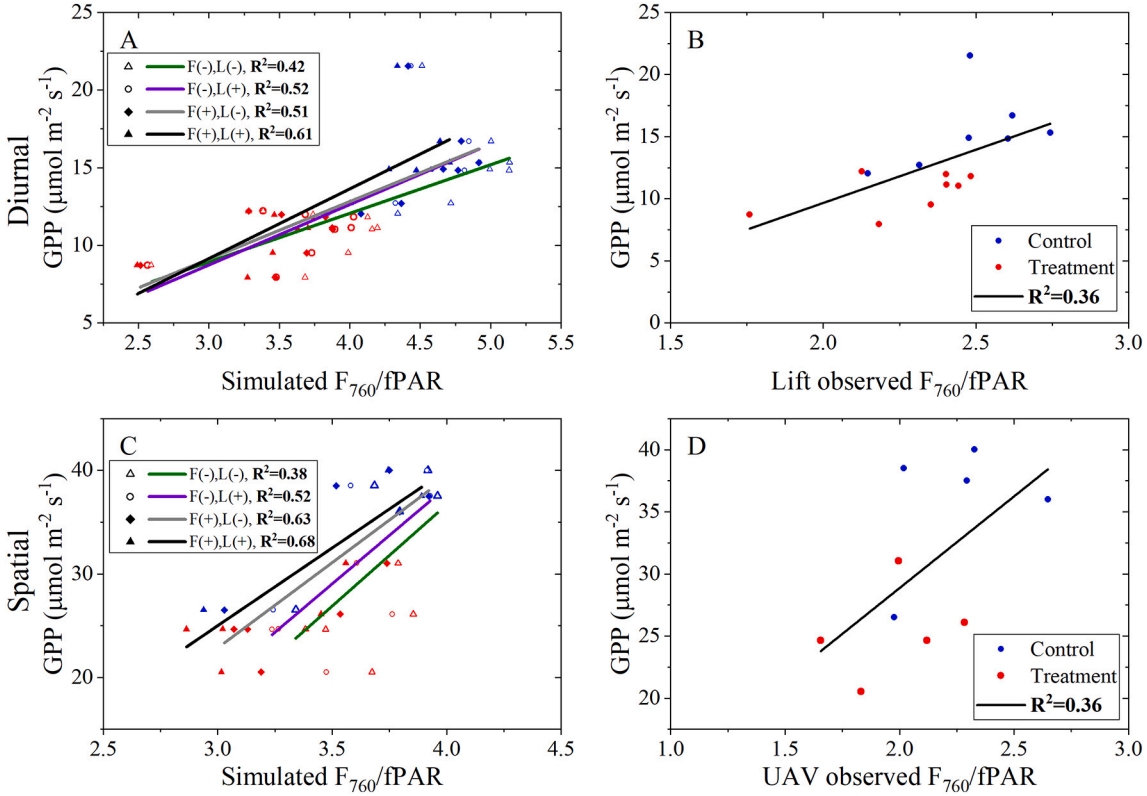

Fig. 10. The impacts of PSII Φ_{F_PSII} (F) and LAD (L) on the diurnal (A, B) and spatial (C, D) relationship between F_{760} and GPP in response to water stress. Diurnal and spatial estimates of leaf-level GPP were derived from stomatal conductance measurements as described in Section 2.3.3. F_{760} scenarios, normalized by fPAR for better comparison with leaf-level GPP, were simulated with SCOPE using different combination of quantum yield of fluorescence in PSII Φ_{F_PSII} (F) and LAD (L) (See Section 2.5). Diurnal and spatial variability of F and L are denoted with symbol '+' and constancy with symbol '-'. Fixed values of F and L were taken from first morning observations (A, diurnal) or from maximum values of F and minimum ALA across experimental plots (C, spatial). The relationship between leaf-level GPP estimates and measured F_{760} in the diurnal and spatial scale are shown in panels B and D, respectively.

ALA, C_{ab}, as well as maximum photochemical efficiencies and fluorescence yield between control and treatment plots (Fig. 4). F_{760} was lower in treatment plots, although this difference was not significant. Possible explanations for the lack of significance include measurement uncertainty in UAV observations and spatial variation of SIF due to heterogeneity in soil properties. Unexpectedly, C_{ab} content, measured in top canopy leaves, was higher in treatment relative to control plots. This observation could indicate certain relocation of mobile nutrients, such as nitrogen, to the younger top canopy leaves promoting increased chlorophyll contents (Yang et al., 2001). In fact, senescence of lower canopy leaves was observed in the treatment plots a few days after measurements supporting this scenario. Overall, our spatial modelling results suggested that the long-term expression of water stress on TOC SIF is mediated by a combination structural and physiological factors, with $APAR_{LAI,Cab}$ explaining the largest proportion of variation in the spatial simulation, followed by Φ_F and LAD-related f_{esc}(Fig. 9). However, we must temper this interpretation based on our empirical observation that almost 90% of total (non-pairwise) spatial variation in far red SIF (F_{760}) was explained by ALA ($R^2 = 0.89$, Fig. B1) with LAI unrelated to F_{760} ($R^2 = 0.01$, not shown). Conversely, and though only calculated over 5 points, plot-wise ΔF_{760} were strongly related to the plot-wise ΔLAI ($R^2 = 0.82$). It is therefore likely that some of the spatial SIF variability assigned to LAI was caused instead by differences in LAD, resulting from limitations in our LAI measurement protocol. Consequently, with more accurate measurements, the role of LAD in Fig. 9 could have been larger, and that of LAI smaller.

4.2. The role of dynamic structure in SIF variation under water stress

In non-woody crops, such as potato, dynamic adjustments in leaf angle or leaf folding help regulate temperature and APAR on daily timescales (Ehleringer and Comstock, 1987; Inoue et al., 2018; Treshow, 1970; Yanovsky et al., 2000). Under drought conditions, non-woody crops are particularly prone to experience noon loss of shoot and leaf turgor, commonly referred to as wilting (Fig. B8), which manifests in terms of LAD changes (Puglielli et al., 2017; Xu et al., 2018).

Leaf inclination, as parametrized by the LAD, has a surprisingly large degree of movement under the influence of leaf turgor and circadian rhythms, which is factor typically overlooked in remote sensing studies of crops. When considered, a (temporally) constant LAD parametrization is usually applied, either inverted from canopy reflectance and/or using default archetypal distributions; for example the spherical type is a popular choice (Hu et al., 2018; van der Tol et al., 2016; Zhang et al., 2018). In this study, photographic methods and particularly the application of a SfM method (Xu et al., 2020) enabled us to retrieve canopy LAD and mean leaf inclination angle difference between treatment and control across spatial and diurnal scales demonstrating the importance of LAD variance in time and space. Using the photographic method, we observed diurnal variation in LAD that was largely coincident with changes in Φ_F and SIF. Diurnal variation was larger in control plots, relative to treatment, although this could be because we missed early morning variation of LAD in treatment plot due to the start time of our diurnal measurements.

In a previous study, Pinto et al. (2017), used a photogrammetric approach, but from a fixed platform, to highlight the importance of leaf inclination angles in controlling spatial variation of SIF imagery in a sugar beet crop. Using UAV-based SfM, we found that LAD was the dominant factor controlling SIF variation across the spatial domain in our experiment (Fig. B1). Critically, and given that LAD dynamics occur concomitantly with physiological adjustments, changes in SIF related to

structural variance run the risk of being mis-interpreted as variance due to Φ_F unless LAD is concomitantly estimated.

Variability in LAD affects TOC SIF via the escape probability, f_{esc}. And as with LAD, f_{esc} estimated from either reflectance indices (NIRv, FCVI) or using simulations varies temporally (Figs. B4, B5). Hence the assumption of static architecture does not hold for potatoes, and likely other crops and woody plants and, if neglected, changes in f_{esc} could be wrongly interpreting in terms of photosynthetic physiology. The fact that diurnal variation in model simulated f_{esc} was less than that in reflectance estimated f_{esc} suggests that there is modelling error related to the canopy radiative transfer processes. Although the diurnal pattern of simulated (normalized) SIF compare well to observed SIF (Fig. 6), this was not the case for simulated diurnal variance in NIR reflectance (data not shown). This issue is not a limitation of SCOPE per se, but a limitation in our application of SCOPE to a non-homogenous canopy. We revisit this issue within the wider context of simulation observation discrepancies in the final section of the discussion (4.4).

4.3. The relative roles of photosynthesis and structure in the relation between SIF and GPP

Our first objective was to characterize the mechanisms behind the diurnal response of SIF under water stress. Our simulations showed a combined response of SIF to Φ_F and LAD in the short-term diurnal data (Fig. 5). Our second objective was to characterize the mechanisms responsible for the spatial response of SIF under water stress. Our results show that structural dynamics, and in particular LAD, played an increasingly important role in mediating spatial SIF variation (Fig. 9, A1). In this section we tackle our final objective, do these changes couple or decouple the relationship between SIF and GPP?

Ideally, if LUE and Φ_F co-vary under the regulation of NPQ and canopy structure is fixed, the relationship between SIF and GPP should also co-vary as shown in Eq. (3). In reality, plants present additional mechanisms to respond to stress, such as photorespiration and leaf angle changes, which can also affect the relationship between SIF and GPP as shown in Fig. 11. According to our conceptual model shown in Fig. 11, GPP is regulated by both NPQ and photorespiration, and canopy SIF is regulated by both Φ_F and f_{esc}, which is related to LAD. Therefore, the relationship between SIF and GPP is affected by dynamic canopy structure and photosynthesis through LUE, Φ_F, and f_{esc}. Based on our results, we argue that changes in dynamic structure effectively couple GPP to SIF, rather than disrupt the relationship.

In this study, leaf level GPP were estimated using leaf level stomatal conductance measurements (section 2.3.3) across a constant leaf area, while SIF was retrieved at the canopy scale under variable LAI. Accordingly, to assess the coupling/decoupling effect of Φ_F and f_{esc} on the relationship between SIF and GPP we normalized SIF by fPAR to exclude the impact of between plot $APAR_{LAI,Cab}$ variation on SIF. Note that we did not measure canopy level GPP but only estimated GPP of top leaves. Accordingly, the purpose of this analysis was not to demonstrate the correlation between SIF and GPP but rather to assess whether short (diurnal cycle) and spatial (long term patterns) adjustments in Φ_F, and LAD induced variation in f_{esc}, couple or decouple SIF from GPP. The results (Fig. 10A, C) demonstrate that the simulated relationship between SIF and GPP improves when measured variation in either Φ_F and LAD are considered, but it is maximal when both the dynamics of Φ_F and LAD are simultaneously considered, demonstrating that both factors strengthen the coupling between SIF and GPP.

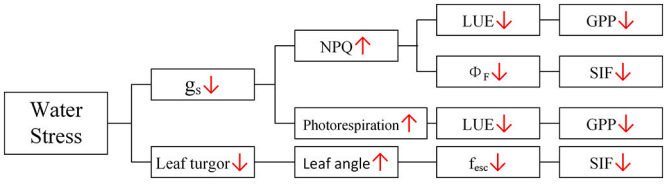

Fig. 11. Schematic of the response of SIF and GPP to drought in a potato crop. Water stress reduces stomatal conductance, increases the rate of photorespiration, and therefore, decreases LUE without a parallel decrease in SIF. This situation will tend to decouple SIF from GPP because GPP decreases by a faster rate than SIF. Water stress causes also a loss of leaf turgor which translates into a reduction in f_{esc} and subsequent decrease in SIF, with no direct effect on GPP. Overall, while separately each of these two mechanisms would decouple SIF from GPP, their decoupling effect tends to cancel out when combined. Accordingly, we hypothesize that the casual interaction between structural and physiological factors acts to retain the coupling between SIF and GPP in response to water stress.

Although canopy SIF and GPP are well correlated at multiple scales (Damm et al., 2015; Guanter et al., 2014; Magney et al., 2019a; Sun et al., 2018), as we show here, assigning photosynthetic causality is problematic due to canopy structural effects which co-vary with physiological adjustments of photosynthesis. This may be an advantage in early warning systems where any drought response is desirable; however more research is needed to better understand the dynamics of structure in satellite data. This effort should start on the ground, with more combined structural and photosynthetic observations across a wider range of species under drought. These observations should be used to test and further develop quantitative models such as SCOPE. In the final discussion section (4.4) we examine limitations of our approach and highlight potential areas of improvement for future studies.

4.4. Accounting for the differences between simulated and measured SIF

In several studies, SCOPE has demonstrated good performance when simulated SIF has been compared to measured values (Celesti et al., 2018; Hu et al., 2018; Migliavacca et al., 2017; van der Tol et al., 2016; Yang et al., 2019). However, simulated SIF in our study was 70% higher than observed SIF. A similar positive bias has also been observed in a water stress study in pine trees by Wohlfahrt et al. (2018) who speculated that the cause was related to the parametrization of fluorescence yields. To a large extent, the mismatch in our study is related to the differences in the selection of the maximum fluorescence yield of PSII.

We assumed a maximum fluorescence yield of PSII of 10% (Appendix C), whereas SCOPE uses a value of 5% (Van der Tol et al., 2014). This change alone will result in doubling the fluorescence emission at the photosystem level and can partly explain the differences. In fact, estimations of this parameter cited in the literature typically range from 7 to 10% (Dau, 1994; Govindje, 1995; Pfündel, 1998) mostly rooted in lifetime studies conducted in the 1950s (Brody and Rabinowitch, 1957). Clearly, this is a critical parameter for SIF modelling studies which deserves further attention. However, this issue has no influence for estimating relative role of Φ_F and LAD in controlling SIF variation using SCOPE model in this study.

There are also a few other explanations for the overestimation. It is possible that SCOPE underestimates the reabsorption of SIF inside the leaf, being based on FLUSPECT/PROSPECT, chlorophyll is homogeneously distributed inside the leaf whereas, in reality, chlorophyll is aggregated into light-harvesting complexes and thylakoids potentially enhancing reabsorption. Additionally, the SCOPE version used here employs a 1D turbid medium model to simulate radiative transfer, hence the effect of the row planting is not considered, and neither is irregular within row clumping of vegetation. Ignoring such structural inhomogeneities could mean that we underestimate the effect of structural parameters on the SIF signal, and potentially overstate the importance of Φ_F in explaining SIF variability. In the current study we chose to use SCOPE as it is the standard tool in the SIF field, however more complex 3D schemes (e.g. FluorWPS, DART) do exist (Liu et al., 2019; Zhao et al., 2016) which could be applied in the future to further investigate the role of structural inhomogeneities on SIF.

There were also factors relating to our retrieval which could have resulted in lower than expected SIF measurements. An instrumental factor which affected our retrievals was the spectral offset and resultant

correction that we applied; an error of approximately 12% was noted in our previous correction analysis based on synthetic data (Atherton et al., 2019).

As we didn't perform atmospheric correction our SIF retrievals were lower than the true TOC values (Sabater et al., 2017). The reason we chose not to correct our data was due to the short path lengths between canopy top and sensors on UAV and lift platforms. We also found no relationship between UAV platform altitude and SIF at either Oxygen feature (data not shown). In addition, UAV retrieved SIF was 0.10 W m^{-2} μm^{-1} sr^{-1} at our bare earth validation plot, implying relatively small retrieval errors. Taken together these results suggest that the influence of the atmosphere was of secondary importance in controlling spatial variation of SIF in our study. Although atmospheric correction is possible for low altitude UAV retrievals (Wang et al., 2021), we reason that more research is needed on this topic before we can confidently apply model-based corrections to very short path lengths.

5. Conclusions

In this study we investigated the drivers of spatial and diurnal SIF variability in response to water stress in a potato crop. We found a combined response of SIF to Φ_F and LAD at the diurnal scale. SIF variation across space, which reflected longer term mechanisms, was dominated by structural factors. Finally, we found that variation in Φ_F and LAD coupled SIF to GPP across water stress and controlled conditions. However, we also found that changes in SIF which relate to structure could potentially be mis-interpreted as relating to Φ_F. We therefore recommend extending the focus on the relationship between canopy structure and SIF to include observations of diurnal and spatial leaf angular variation utilizing the field measurement approaches presented here.

Declaration of Competing Interest

None.

Acknowledgements

This work was supported by the Academy of Finland (grant numbers 288039, 319211, 304097). Shan Xu was also supported by the China Scholarship Council (CSC) under grant 201806040163, and by the Natural Science Foundation of China (grant number 42071402) during this work.

Author statement

Shan Xu: Conceptualization, Methodology, Formal analysis, Writing - original draft, Writing - review & editing, Visualization. **Jon Atherton:** Conceptualization, Methodology, Formal analysis, Writing - original draft, Writing - review & editing. **Anu Riikonen:** Data curation, Writing - review & editing. **Chao Zhang:** Data curation, Writing - review & editing. **Jaakko Oivukkamäki:** Data curation, Writing - review & editing. **Alasdair MacArthur:** Methodology, Writing - review & editing. **Eija Honkavaara:** Methodology, Writing - review & editing. **Teemu Hakala:** Methodology, Data curation. **Niko Viljanen:** Methodology, Data curation. **Zhigang Liu:** Writing - review & editing. **Albert Porcar-Castell:** Conceptualization, Methodology, Formal analysis, Writing - original draft, Writing - review & editing, Funding acquisition.

Declaration of Competing Interest

The authors declare that they have no known competing financial interests or personal relationships that could have appeared to influence the work reported in this paper.

Appendix A. Supplementary data

Supplementary data to this article can be found online at https://doi.org/10.1016/j.rse.2021.112555.

The datasets used to prepare the figures of this study are available from: https://zenodo.org/record/4607784#.YMCNKjqEZFQ. The doi associated with this dataset is 10.5281/zenodo.4607784. Please contact the authors if you plan to use the data.

References

Alley, W.M., 1984. The palmer drought severity index: limitations and assumptions. J. Appl. Meteorol. Climatol. 23, 1100–1109. https://doi.org/10.1175/1520-0450(1984)023<1100:TPDSIL>2.0.CO;2.

Alonso, L., Van Wittenberghe, S., Amorós-López, J., Vila-Francés, J., Gómez-Chova, L., Moreno, J., 2017. Diurnal cycle relationships between passive fluorescence, PRI and NPQ of vegetation in a controlled stress experiment. Remote Sens. 9, 770.

Atherton, J., MacArthur, A., Hakala, T., Maseyk, K., Robinson, I., Liu, W., Honkavaara, E., Porcar-Castell, A., 2018. Drone measurements of solar-induced chlorophyll fluorescence acquired with a low-weight DFOV spectrometer system. In: IGARSS 2018–2018 IEEE International Geoscience and Remote Sensing Symposium, pp. 8834–8836. https://doi.org/10.1109/IGARSS.2018.8517474.

Atherton, J., Xu, S., Porcar-Castell, A., 2019. Heuristic methods to correct for wavelength offset effects in dual field of view spectrometer systems. In: Proceedings of the Center of Excellence in Atmospheric Science (CoE ATM) Annual Seminar 2019. Finnish Association for Aerosol Research FAAR, pp. 169–171.

Baker, N.R., 2008. Chlorophyll fluorescence: a probe of photosynthesis in vivo. Annu. Rev. Plant Biol. 59, 89–113.

Ball, J.T., Woodrow, I.E., Berry, J.A., 1987. A Model Predicting Stomatal Conductance and its Contribution to the Control of Photosynthesis under Different Environmental Conditions, in: Progress in Photosynthesis Research. https://doi.org/10.1007/978-94-017-0519-6_48.

Brody, S., Rabinowitch, E., 1957. Excitation lifetime of photosynthetic pigments in vitro and in vivo. Science (80-.) 125. https://doi.org/10.1126/science.125.3247.555, 555 LP – 555.

Celesti, M., van der Tol, C., Cogliati, S., Panigada, C., Yang, P., Pinto, F., Rascher, U., Miglietta, F., Colombo, R., Rossini, M., 2018. Exploring the physiological information of Sun-induced chlorophyll fluorescence through radiative transfer model inversion. Remote Sens. Environ. 215, 97–108.

Cendrero-Mateo, M.P., Carmo-Silva, A.E., Porcar-Castell, A., Hamerlynck, E.P., Papuga, S.A., Moran, M.S., 2015. Dynamic response of plant chlorophyll fluorescence to light, water and nutrient availability. Funct. Plant Biol. 42, 746–757.

Damm, A., Guanter, L., Paul-Limoges, E., Van der Tol, C., Hueni, A., Buchmann, N., Eugster, W., Ammann, C., Schaepman, M.E., 2015. Far-red sun-induced chlorophyll fluorescence shows ecosystem-specific relationships to gross primary production: an assessment based on observational and modeling approaches. Remote Sens. Environ. 166, 91–105.

Dau, H., 1994. Molecular mechanisms and quantitative models of variable photosystem II fluorescence. Photochem. Photobiol. 60, 1–23. https://doi.org/10.1111/j.1751-1097.1994.tb03937.x.

Dechant, B., Ryu, Y., Badgley, G., Zeng, Y., Berry, J.A., Zhang, Y., Goulas, Y., Li, Z., Zhang, Q., Kang, M., Li, J., Moya, I., 2020. Canopy structure explains the relationship between photosynthesis and sun-induced chlorophyll fluorescence in crops. Remote Sens. Environ. 241, 111733. https://doi.org/10.1016/J.RSE.2020.111733.

Ehleringer, J.R., Comstock, J., 1987. Leaf absorptance and leaf angle: mechanisms for stress avoidance. In: Plant Response to Stress. Springer, pp. 55–76.

Farquhar, G.D., Von Caemmerer, S., Berry, J.A., 1980. A biochemical model of photosynthetic CO2 assimilation in leaves of C3 species. Planta 149, 78–90.

Flexas, J., Briantais, J.-M., Cerovic, Z., Medrano, H., Moya, I., 2000. Steady-state and maximum chlorophyll fluorescence responses to water stress in grapevine leaves: a new remote sensing system. Remote Sens. Environ. 73, 283–297.

Flexas, J., Escalona, J.M., Evain, S., Gulías, J., Moya, I., Osmond, C.B., Medrano, H., 2002. Steady-state chlorophyll fluorescence (fs) measurements as a tool to follow variations of net CO2 assimilation and stomatal conductance during water-stress in C3 plants. Physiol. Plant. 114, 231–240.

Frankenberg, C., Berry, J., 2018. Solar Induced Chlorophyll Fluorescence: Origins, Relation to Photosynthesis and Retrieval.

Govindje, E., 1995. Sixty-three years since Kautsky: chlorophyll a fluorescence. Funct. Plant Biol. 22, 131–160.

Guanter, L., Zhang, Y., Jung, M., Joiner, J., Voigt, M., Berry, J.A., Frankenberg, C., Huete, A.R., Zarco-Tejada, P., Lee, J.-E., Moran, M.S., Ponce-Campos, G., Beer, C., Camps-Valls, G., Buchmann, N., Gianelle, D., Klumpp, K., Cescatti, A., Baker, J.M., Griffis, T.J., 2014. Global and time-resolved monitoring of crop photosynthesis with chlorophyll fluorescence. Proc. Natl. Acad. Sci. 111 https://doi.org/10.1073/pnas.1320008111. E1327 LP-E1333.

Helm, L.T., Shi, H., Lerdau, M.T., Yang, X., 2020. Solar-induced chlorophyll fluorescence and short-term photosynthetic response to drought. Ecol. Appl. 30, e02101 https://doi.org/10.1002/eap.2101.

Hu, J., Liu, X., Liu, L., Guan, L., 2018. Evaluating the performance of the SCOPE model in simulating canopy solar-induced chlorophyll fluorescence. Remote Sens. 10, 250. https://doi.org/10.3390/rs10020250.

Huang, D., Knyazikhin, Y., Dickinson, R.E., Rautiainen, M., Stenberg, P., Disney, M., Lewis, P., Cescatti, A., Tian, Y., Verhoef, W., Martonchik, J.V., Myneni, R.B., 2007. Canopy spectral invariants for remote sensing and model applications. Remote Sens. Environ. 106, 106–122. https://doi.org/10.1016/J.RSE.2006.08.001.

Inoue, K., Araki, T., Endo, M., 2018. Circadian clock during plant development. J. Plant Res. 131, 59–66. https://doi.org/10.1007/s10265-017-0991-8.

Jonasson, S., 1988. Evaluation of the point intercept method for the estimation of plant biomass. Oikos 52, 101. https://doi.org/10.2307/3565988.

Liu, W., Atherton, J., Mõttus, M., Gastellu-Etchegorry, J.-P., Malenovský, Z., Raumonen, P., Åkerblom, M., Mäkipää, R., Porcar-Castell, A., 2019. Simulating solar-induced chlorophyll fluorescence in a boreal forest stand reconstructed from terrestrial laser scanning measurements. Remote Sens. Environ. 232, 111274. https://doi.org/10.1016/J.RSE.2019.111274.

MacArthur, A., Robinson, I., Rossini, M., Davis, N., MacDonald, K., 2014. A Dual-Field-of-View Spectrometer System for Reflectance and Fluorescence Measurements (Piccolo Doppio) and Correction of Etaloning.

Magney, T.S., Bowling, D.R., Logan, B.A., Grossmann, K., Stutz, J., Blanken, P.D., Burns, S.P., Cheng, R., Garcia, M.A., Köhler, P., Lopez, S., Parazoo, N.C., Raczka, B., Schimel, D., Frankenberg, C., 2019a. Mechanistic evidence for tracking the seasonality of photosynthesis with solar-induced fluorescence. Proc. Natl. Acad. Sci. U. S. A. 116, 11640–11645. https://doi.org/10.1073/pnas.1900278116.

Magney, T.S., Frankenberg, C., Köhler, P., North, G., Davis, T.S., Dold, C., Dutta, D., Fisher, J.B., Grossmann, K., Harrington, A., 2019b. Disentangling changes in the spectral shape of chlorophyll fluorescence: implications for remote sensing of photosynthesis. J. Geophys. Res. Biogeosci. 124, 1491–1507.

Magney, T.S., Barnes, M.L., Yang, X., 2020. On the covariation of chlorophyll fluorescence and photosynthesis across scales. Geophys. Res. Lett. 47 (e2020GL091098).

Mänd, P., Hallik, L., Peñuelas, J., Nilson, T., Duce, P., Emmett, B.A., Beier, C., Estiarte, M., Garadnai, J., Kalapos, T., Schmidt, I.K., Kovács-Láng, E., Prieto, P., Tietema, A., Westerveld, J.W., Kull, O., 2010. Responses of the reflectance indices PRI and NDVI to experimental warming and drought in European shrublands along a north-south climatic gradient. Remote Sens. Environ. 114, 626–636. https://doi.org/10.1016/j.rse.2009.11.003.

Marrs, J.K., Reblin, J.S., Logan, B.A., Allen, D.W., Reinmann, A.B., Bombard, D.M., Tabachnik, D., Hutyra, L.R., 2020. Solar-induced fluorescence does not track photosynthetic carbon assimilation following induced stomatal closure. Geophys. Res. Lett. 47, e2020GL087956 https://doi.org/10.1029/2020GL087956.

Martini, D., Pacheco-Labrador, J., Perez-Priego, O., van der Tol, C., El-Madany, T.S., Julitta, T., Rossini, M., Reichstein, M., Christiansen, R., Rascher, U., Moreno, G., Martín, M.P., Yang, P., Carrara, A., Guan, J., González-Cascón, R., Migliavacca, M., 2019. Nitrogen and phosphorus effect on Sun-induced fluorescence and gross primary productivity in Mediterranean grassland. Remote Sens. https://doi.org/10.3390/rs11212562.

Maxwell, K., Johnson, G.N., 2000. Chlorophyll fluorescence—a practical guide. J. Exp. Bot. 51, 659–668. https://doi.org/10.1093/jexbot/51.345.659.

Meroni, M., Busetto, L., Colombo, R., Guanter, L., Moreno, J., Verhoef, W., 2010. Performance of spectral fitting methods for vegetation fluorescence quantification. Remote Sens. Environ. 114, 363–374.

Miao, G., Guan, K., Yang, X., Bernacchi, C.J., Berry, J.A., DeLucia, E.H., Wu, J., Moore, C. E., Meacham, K., Cai, Y., Peng, B., Kimm, H., Masters, M.D., 2018. Sun-induced chlorophyll fluorescence, photosynthesis, and light use efficiency of a soybean field from seasonally continuous measurements. J. Geophys. Res. Biogeosci. 123, 610–623. https://doi.org/10.1002/2017JG004180.

Migliavacca, M., Perez-Priego, O., Rossini, M., El-Madany, T.S., Moreno, G., van der Tol, C., Rascher, U., Berninger, A., Bessenbacher, V., Burkart, A., Carrara, A., Fava, F., Guan, J.-H., Hammer, T.W., Henkel, K., Juarez-Alcalde, E., Julitta, T., Kolle, O., Martín, M.P., Musavi, T., Pacheco-Labrador, J., Pérez-Burgueño, A., Wutzler, T., Zaehle, S., Reichstein, M., 2017. Plant functional traits and canopy structure control the relationship between photosynthetic CO2 uptake and far-red sun-induced fluorescence in a Mediterranean grassland under different nutrient availability. New Phytol. 214, 1078–1091. https://doi.org/10.1111/nph.14437.

Monteith, J.L., 1972. Solar radiation and productivity in tropical ecosystems. J. Appl. Ecol. 9, 747–766. https://doi.org/10.2307/2401901.

Obidiegwu, J.E., Bryan, G.J., Jones, H.G., Prashar, A., 2015. Coping with drought: stress and adaptive responses in potato and perspectives for improvement. Front. Plant Sci. 6, 542. https://doi.org/10.3389/fpls.2015.00542.

Olesen, J.E., Trnka, M., Kersebaum, K.-C., Skjelvåg, A.O., Seguin, B., Peltonen-Sainio, P., Rossi, F., Kozyra, J., Micale, F., 2011. Impacts and adaptation of European crop production systems to climate change. Eur. J. Agron. 34, 96–112.

Pfündel, E., 1998. Estimating the contribution of photosystem I to total leaf chlorophyll fluorescence. Photosynth. Res. 56, 185–195. https://doi.org/10.1023/A:1006032804606.

Pinto, F., Müller-Linow, M., Schickling, A., Cendrero-Mateo, M.P., Ballvora, A., Rascher, U., 2017. Multiangular observation of canopy Sun-induced chlorophyll fluorescence by combining imaging spectroscopy and stereoscopy. Remote Sens. https://doi.org/10.3390/rs9050415.

Pisek, J., Ryu, Y., Alikas, K., 2011. Estimating leaf inclination and G-function from leveled digital camera photography in broadleaf canopies. Trees 25, 919–924. https://doi.org/10.1007/s00468-011-0566-6.

Porcar-Castell, A., Mac Arthur, A., Rossini, M., Eklundh, L., Pacheco-Labrador, J., Anderson, K., Balzarolo, M., Martín, M.P., Jin, H., Tomelleri, E., Cerasoli, S., Sakowska, K., Hueni, A., Julitta, T., Nichol, C.J., Vescovo, L., 2015. EUROSPEC: at the interface between remote-sensing and ecosystem CO_2 flux measurements in Europe. Biogeosciences 12, 6103–6124. https://doi.org/10.5194/bg-12-6103-2015.

Porcar-Castell, A., Tyystjärvi, E., Atherton, J., van der Tol, C., Flexas, J., Pfündel, E.E., Moreno, J., Frankenberg, C., Berry, J.A., 2014. Linking chlorophyll a fluorescence to photosynthesis for remote sensing applications: mechanisms and challenges. J. Exp. Bot. 65, 4065–4095. https://doi.org/10.1093/jxb/eru191.

Puglielli, G., Gratani, L., Varone, L., 2017. Leaf rolling as indicator of water stress in Cistus incanus; from different provenances. bioRxiv 131508. https://doi.org/10.1101/131508.

Reynolds-Henne, C.E., Langenegger, A., Mani, J., Schenk, N., Zumsteg, A., Feller, U., 2010. Interactions between temperature, drought and stomatal opening in legumes. Environ. Exp. Bot. doi. https://doi.org/10.1016/j.envexpbot.2009.11.002.

Sabater, N., Middleton, E.M., Malenovsky, Z., Alonso, L., Verrelst, J., Huemmrich, K.F., Campbell, P.K.E., Kustas, W.P., Vicent, J., Van Wittenberghe, S., 2017. Oxygen transmittance correction for solar-induced chlorophyll fluorescence measured on proximal sensing: Application to the NASA-GSFC fusion tower. In: Geoscience and Remote Sensing Symposium (IGARSS), 2017 IEEE International. IEEE, pp. 5826–5829.

Sharp, R.E., Matthews, M.A., Boyer, J.S., 1984. Kok effect and the quantum yield of photosynthesis. Plant Physiol. 75 https://doi.org/10.1104/pp.75.1.95, 95 LP – 101.

Sun, Y., Fu, R., Dickinson, R., Joiner, J., Frankenberg, C., Gu, L., Xia, Y., Fernando, N., 2015. Drought onset mechanisms revealed by satellite solar-induced chlorophyll fluorescence: insights from two contrasting extreme events. J. Geophys. Res. Biogeosci. 120, 2427–2440.

Sun, Y., Frankenberg, C., Jung, M., Joiner, J., Guanter, L., Köhler, P., Magney, T., 2018. Overview of solar-induced chlorophyll fluorescence (SIF) from the orbiting carbon Observatory-2: retrieval, cross-mission comparison, and global monitoring for GPP. Remote Sens. Environ. 209, 808–823. https://doi.org/10.1016/J.RSE.2018.02.016.

Treshow, M., 1970. Environment & plant response. McGraw-Hill publications in the agricultural sciences, McGraw-Hill.

Van der Tol, C., Verhoef, W., Rosema, A., 2009. A model for chlorophyll fluorescence and photosynthesis at leaf scale. Agric. For. Meteorol. 149, 96–105.

Van der Tol, C., Berry, J.A., Campbell, P.K.E., Rascher, U., 2014. Models of fluorescence and photosynthesis for interpreting measurements of solar-induced chlorophyll fluorescence. J. Geophys. Res. Biogeosci. 119, 2312–2327.

van der Tol, C., Rossini, M., Cogliati, S., Verhoef, W., Colombo, R., Rascher, U., Mohammed, G., 2016. A model and measurement comparison of diurnal cycles of sun-induced chlorophyll fluorescence of crops. Remote Sens. Environ. 186, 663–677.

Verhoef, W., 1998. Theory of radiative transfer models applied in optical remote sensing of vegetation canopies. Wageningen Agricultural University (Doi: ISBNL 90-5485-804-4).

Viljanen, N., Honkavaara, E., Näsi, R., Hakala, T., Niemeläinen, O., Kaivosoja, J., 2018. A novel machine learning method for estimating biomass of grass swards using a photogrammetric canopy height model, images and vegetation indices captured by a drone. Agriculture. https://doi.org/10.3390/agriculture8050070.

Viña, A., Gitelson, A.A., 2005. New developments in the remote estimation of the fraction of absorbed photosynthetically active radiation in crops. Geophys. Res. Lett. doi. https://doi.org/10.1029/2005GL023647.

Walker, T.S., Schmiediche, P.E., Hijmans, R.J., 1999. World trends and patterns in the potato crop: an economic and geographic survey. Potato Res. 42, 241–264. https://doi.org/10.1007/BF02357856.

Wang, N., Suomalainen, J., Bartholomeus, H., Kooistra, L., Masiliūnas, D., Clevers, J.G.P. W., 2021. Diurnal variation of sun-induced chlorophyll fluorescence of agricultural crops observed from a point-based spectrometer on a UAV. Int. J. Appl. Earth Obs. Geoinf. 96, 102276.

Wardlow, B.D., Tadesse, T., Brown, J.F., Callahan, K., Swain, S., Hunt, E., 2012. Vegetation Drought Response Index an Integration of Satellite, Climate, and Biophysical Data.

Wellburn, A.R., 1994. The spectral determination of chlorophylls a and b, as well as Total carotenoids, Using Various Solvents with Spectrophotometers of Different Resolution. J. Plant Physiol. 144, 307–313. https://doi.org/10.1016/S0176-1617(11)81192-2.

Wohlfahrt, G., Gerdel, K., Migliavacca, M., Rotenberg, E., Tatarinov, F., Müller, J., Hammerle, A., Julitta, T., Spielmann, F.M., Yakir, D., 2018. Sun-induced fluorescence and gross primary productivity during a heat wave. Sci. Rep. 8, 14169. https://doi.org/10.1038/s41598-018-32602-z.

Xu, S., Liu, Z., Zhao, L., Zhao, H., Ren, S., 2018. Diurnal response of Sun-induced fluorescence and PRI to water stress in maize using a near-surface remote sensing platform. Remote Sens. 10, 1510.

Xu, S., Zaidan, M.A., Honkavaara, E., Hakala, T., Viljanen, N., Porcar-Castell, A., Liu, Z., Atherton, J., 2020. On the estimation of the leaf angle distribution from drone based photogrammetry. In: IGARSS 2020–2020 IEEE International Geoscience and Remote Sensing Symposium, pp. 4379–4382. https://doi.org/10.1109/IGARSS39084.2020.9323498.

Yang, P., van der Tol, C., Verhoef, W., Damm, A., Schickling, A., Kraska, T., Muller, O., Rascher, U., 2019. Using reflectance to explain vegetation biochemical and structural effects on sun-induced chlorophyll fluorescence. Remote Sens. Environ. 231, 110996. https://doi.org/10.1016/J.RSE.2018.11.039.

Yang, P., van der Tol, C., Campbell, P.K.E., Middleton, E.M., 2020. Fluorescence correction vegetation index (FCVI): a physically based reflectance index to separate physiological and non-physiological information in far-red sun-induced chlorophyll fluorescence. Remote Sens. Environ. 240, 111676.

Yang, P., van der Tol, C., Campbell, P.K.E., Middleton, E.M., 2021. Unraveling the physical and physiological basis for the solar-induced chlorophyll fluorescence and photosynthesis relationship using continuous leaf and canopy measurements of a corn crop. Biogeosciences 18, 441–465.

Yang, J., Zhang, J., Wang, Z., Zhu, Q., Liu, L., 2001. Water deficit-induced senescence and its relationship to the remobilization of pre-stored carbon in wheat during grain filling. Agron. J. 93, 196–206. https://doi.org/10.2134/agronj2001.931196x.

Yanovsky, M.J., Izaguirre, M., Wagmaister, J.A., Gatz, C., Jackson, S.D., Thomas, B., Casal, J.J., 2000. Phytochrome a resets the circadian clock and delays tuber formation under long days in potato. Plant J. 23, 223–232. https://doi.org/10.1046/j.1365-313x.2000.00775.x.

Zarco-Tejada, P.J., Berni, J.A.J., Suárez, L., Sepulcre-Cantó, G., Morales, F., Miller, J.R., 2009. Imaging chlorophyll fluorescence with an airborne narrow-band multispectral camera for vegetation stress detection. Remote Sens. Environ. 113, 1262–1275.

Zeng, Y., Badgley, G., Dechant, B., Ryu, Y., Chen, M., Berry, J.A., 2019. A practical approach for estimating the escape ratio of near-infrared solar-induced chlorophyll fluorescence. Remote Sens. Environ. 232, 111209.

Zhang, L., Xiao, J., Zhou, Y., Zheng, Y., Li, J., Xiao, H., 2016. Drought events and their effects on vegetation productivity in China. Ecosphere 7, e01591.

Zhang, Yao, Xiao, X., Zhang, Yongguang, Wolf, S., Zhou, S., Joiner, J., Guanter, L., Verma, M., Sun, Y., Yang, X., Paul-Limoges, E., Gough, C.M., Wohlfahrt, G., Gioli, B., van der Tol, C., Yann, N., Lund, M., de Grandcourt, A., 2018. On the relationship between sub-daily instantaneous and daily total gross primary production: implications for interpreting satellite-based SIF retrievals. Remote Sens. Environ. 205, 276–289. https://doi.org/10.1016/j.rse.2017.12.009.

Zhang, L., Qiao, N., Huang, C., Wang, S., 2019. Monitoring drought effects on vegetation productivity using satellite solar-induced chlorophyll fluorescence. Remote Sens. 11, 378. https://doi.org/10.3390/rs11040378.

Zhang, Z., Zhang, Y., Porcar-Castell, A., Joiner, J., Guanter, L., Yang, X., Migliavacca, M., Ju, W., Sun, Z., Chen, S., Martini, D., Zhang, Q., Li, Z., Cleverly, J., Wang, H., Goulas, Y., 2020. Reduction of structural impacts and distinction of photosynthetic pathways in a global estimation of GPP from space-borne solar-induced chlorophyll fluorescence. Remote Sens. Environ. 240, 111722. https://doi.org/10.1016/j.rse.2020.111722.

Zhao, F., Dai, X., Verhoef, W., Guo, Y., van der Tol, C., Li, Y., Huang, Y., 2016. FluorWPS: a Monte Carlo ray-tracing model to compute sun-induced chlorophyll fluorescence of three-dimensional canopy. Remote Sens. Environ. 187, 385–399. https://doi.org/10.1016/j.rse.2016.10.036.